"Branched" structural transformation of the $L1_2$-Al_3Zr phase manipulated by Cu substitution/segregation in the Al-Cu-Zr alloy system

Lipeng Ding[a], Mingqi Zhao[b], Flemming J. H. Ehlers[a], Zhihong Jia[a*], Zezhong Zhang[c,d], Yaoyao Weng[e], Dominique Schryvers[c], Qing Liu[a], Hosni Idrissi[f,c]

[a] Key laboratory for Light-weight Materials, Nanjing Tech University, Nanjing 211816, China

[b] School of Automation, Chongqing University of Posts and Telecommunications, Chongqing 400065, China

[c] Electron Microscopy for Materials Science (EMAT), Department of Physics, University of Antwerp, Groenenborgerlaan 171, B-2020, Belgium

[d] Department of Materials, University of Oxford, Oxford, 1OX 3PH, UK

[e] School of Materials Science and Engineering, Nanjing Institute of Technology, Nanjing 211167, China

[f] UCLouvain, Institute of Mechanics, Materials and Civil Engineering, IMAP, 1348 Louvain-la-Neuve, Belgium

*Corresponding author.

Zhihong Jia, E-mail: zhihongjia@njtech.edu.cn, Tel.: +86-25-83589187;

Abstract

The effect of Cu on the evolution of the Al_3Zr phase in an Al-Cu-Zr cast alloy during solution treatment at 500 °C has been thoroughly studied by combining atomic resolution high-angle annular dark-field scanning transmission electron microscopy, energy-dispersive X-ray spectroscopy and first-principles calculations. The heat treatment initially produces a pure $L1_2$-Al_3Zr microstructure, allowing for about 13% Cu to be incorporated on the Al sublattice of the dispersoid. Cu incorporation reduces the lattice misfit between the $L1_2$ and Al matrix and increases the energy barrier for

anti-phase boundary (APB) activation, thus stabilizing the $L1_2$ structure. Additional heating leads to a Cu-induced "branched" path for the $L1_2$ structural transformation, with the latter process accelerated once the first APB has been created. Cu atoms may either (i) be repelled by the APBs, promoting the transformation to a Cu-poor $D0_{23}$ phase, or (ii) they may segregate at one Al-Zr layer adjacent to the APB, promoting a transformation to a new thermodynamically favored phase, Al_4CuZr, formed when these segregation layers are periodically arranged. Theoretical studies suggest that the branching of the $L1_2$ transformation path is linked to the speed at which an APB is created, with Cu attraction triggered by a comparatively slow process. This unexpected transformation behavior of the $L1_2$-Al_3Zr phase opens a new path to understanding, and potentially regulating the Al_3Zr dispersoid evolution for high temperature applications.

Key words: Aluminum alloys; Trialuminides; Anti-phase boundary; High-angle annular dark-field scanning transmission electron microscopy (HAADF-STEM); First-principles calculations

1. Introduction

The intermetallic compounds of Al_3X (X = Zr, Sc, Er, etc.) have long been a subject of interest due to their attractive properties, such as high specific strengths at both ambient and elevated temperatures, relatively low densities, good oxidation resistances, and high melting points, making them ideal candidates for developing high-temperature creep-resistant Al-based alloys [1-3]. Among the various kinds of Al_3X phases, there is a special interest in the Al_3Zr phase because of the low solid solubility and sluggish diffusion rate of Zr in Al, the good coherency of Al_3Zr with the Al matrix and low production cost. During the annealing treatment of the Al-Zr alloy system, elastically hard and coherent Al_3Zr dispersoids with an $L1_2$ structure are formed, which interact with dislocations and thus effectively inhibit recrystallization and the corresponding strength loss during heat exposure [4-6].

However, the metastable $L1_2$-Al_3Zr phase can transform into the equilibrium

$D0_{23}$ phase during aging above 450 °C [7]. Unfortunately, the $D0_{23}$ phase is semi-coherent with the Al matrix and exhibits inherent brittleness due to its low structural symmetry and limited equivalent slip systems, which results in a significant decrease of strength and ductility [8-10]. Stabilizing Al_3Zr in the $L1_2$ structure is thus essential for the thermal stability of this class of alloys. Several research groups have studied the precipitation evolution of the Al_3Zr phase and proposed that anti-phase boundaries (APBs) are the key defects involved in the $L1_2 \rightarrow D0_{23}$ transition [4, 8, 11, 12]. This is supported by the $D0_{23}$ phase differing from $L1_2$ by introduction of a periodic arrangement of such APBs [8]. Knipling et al. [13] reported that the introduction of an APB with a displacement vector a/2<110> on {100} planes indicates the early stage of the transformation. It has also been reported that the Al-X bonds in the trialuminides Al_3X are notably covalent, with the $D0_{23}$-$L1_2$ relative stability being highly sensitive to the identity of element X [3, 14, 15]. Micro-alloying can thus be used to stabilize the $L1_2$ phase. Alloy strengthening by the $L1_2$ phase requires to keep coarsening low, aided by reduction of the lattice mismatch between precipitate and matrix and a low diffusivity of the solute atoms involved.

Two different groups of micro-alloying elements can be distinguished depending on their substitution positions [16, 17]. The first type of elements (Sc, Ti, V, Hf, Er, Tm, Yb, Lu etc.) enters the Zr sites of Al_3Zr. The partial substitution of Zr leads to the formation of ternary or quaternary trialuminide compounds, which leads to a reduction in the lattice parameter mismatch and interfacial free energy of Al_3Zr with the matrix and/or an improved stability of $L1_2$ relative to $D0_{23}$, thus promoting the coarsening resistance and thermal stability of the particles [18-20]. Clouet et al. [21] reported that the combined addition of Sc and Zr to Al alloys leads to the formation of $L1_2$-structured $Al_3(Sc_{1-x}Zr_x)$, consisting of a Sc-enriched core and a Zr-enriched shell, with greatly improved thermal stability over $L1_2$-Al_3Zr. Zhang et al. [22] reported that the addition of 0.03 at.% Yb in an Al-Zr alloy leads to a significant precipitation strengthening and thermal stability, which was attributed to a reduced lattice parameter mismatch between the $Al_3(Zr_{1-x}Yb_x)$ dispersoids and the matrix. However, the high cost of Sc or Yb limits their use.

The second type of micro-alloying elements could be Li, Cu, Mg, Zn, Cr, Fe, Co, Ni and Ag (see, e.g., Dorin et al. and Srinivasan et al. [23, 24]). In this case, the added element enters the Al sites in Al_3Zr. The addition of these elements has gained particular attention in the last years due to their promising ability for increasing precipitation hardening and thermal stability of the Al_3Zr dispersoids. Dorin et al. [23] showed that Si incorporation in Al_3Zr induces accelerated precipitation in the alloy. By using an integrated modelling approach, Robson et al. [25] predicted that Cu, Mg and Zn additions can shift the solvus of Al_3Zr to low Zr concentrations, once again promoting the phase precipitation kinetics. Desch et al. [26] reported that the addition of Li and Cr increases the stability of the $L1_2$ phase to 750 °C and 740 °C, respectively, while the addition of Fe and Ni would lead to the formation of an amorphous phase, rather than $L1_2$. On the other hand, the addition of Cu was reported to increase the $L1_2$ phase stability to at least 1300 °C [26], which increases the attention paid to this element. Jia et al. [27] reported that the addition of Cu in an Al-Zr alloy induces significant increase of strength due to a dense distribution of the Al_3Zr dispersoids. Cassell et al. [28] studied the dispersoid composition in a Zr-containing AA7010 aluminum alloy (0.76 at.% Cu), and reported Cu incorporation of up to 5% (along with Zn) in the $L1_2$-Al_3Zr dispersoid when heating at 485 °C for 1h. Schmid et al. [29] studied the high temperature stability of the $L1_2$-Al_3Zr dispersoids with ternary element addition. For the case of Cu, an alloy concentration of 1.43 at.% was found to be associated with only very weak Cu incorporation in $L1_2$-Al_3Zr at 475 °C. When heating at 550 °C, the dispersoids transformed to the $D0_{23}$ structure, and Cu was entirely expelled, forming separate, attached particles. Contrasting these findings, Hu et al. [30] reported $L1_2$ dispersoids with composition $Al_{2.5}Cu_{0.5}Zr$ following heating at 500 °C for 26h of an alloy with 2.55 at.% Cu. At the end of the aging treatment, the particle dimensions clearly exceeded earlier reported [9] coherency loss threshold values for dispersoids in the Al-Zr system.

Theoretical studies probing the Cu influence on $L1_2$-Al_3Zr are sparse. Cassell et al. [28] suggested that Cu incorporation in the dispersoid should be promoted in alloys with a Cu concentration somewhat above 1 at.%. Hu et al. [30] showed that

even a few percent of Cu on the Al sublattice in $L1_2$-Al_3Zr would be sufficient to stabilize this phase over (Cu-containing) $D0_{23}$, indicating that Cu indeed hinders APB formation. The latter conclusion is supported by more recent calculations by Schmid et al. [29]. To the best of the author's knowledge, a complete study of the influence of Cu concentration on the APB energy barrier characteristics is still absent in the literature. Several questions remain regarding the Cu incorporation in the dispersoids as well as the critical amount of Cu required to trigger interesting effects. Furthermore, the lack of detailed theoretical and experimental studies on the influence of Cu on the early stages of the $L1_2 \rightarrow D0_{23}$ transition still constitutes an obstacle for better understanding of this phenomena. This also prevents optimization of the chemical compositions, heat treatment processes and thus the mechanical properties of Al-Zr based alloys with Cu.

In the present work, the structural evolution of the Al_3Zr phase in an Al-Cu-Zr alloy is systematically studied by aberration-corrected scanning transmission electron microscopy (STEM), energy-dispersive X-ray spectroscopy (EDX) and first-principles density functional theory (DFT) calculations. In the alloy under investigation, Cu is found to be incorporated on the Al sublattice in $L1_2$-Al_3Zr when heating at 500 °C, in concentrations supporting [30]. Following long-term heating (beyond 100h), Cu is found to segregate in the vicinity of an isolated APB, whereby the transition to a new Cu-containing phase (composition Al_4CuZr) hosting a periodic arrangement of Cu segregation layers is initiated. This unknown precipitate evolution path takes place alongside the 'standard' $L1_2 \rightarrow D0_{23}$ transition where Cu is repelled by the APB, emphasizing the importance of the circumstances under which the APBs are created. Theoretical investigations elaborated on this highly dynamic response of Cu to APB creation confirms the key role of the speed at which this extended defect is formed in the Al_4CuZr nucleation. These findings provide new information for better understanding of the Al_3Zr dispersoid evolution in response to Cu micro-alloying. The newly identified transformation path could also play a role in other trialuminides with different micro-alloying elements.

2. Materials and methods

2.1 Experiments

An alloy with nominal composition of Al–5.0%Cu–0.2%Zr (wt.%) was used for all experimental investigations. The Al-Cu-Zr alloy was cast into a cylindrical bar by the direct chill method using pure Al (99.99 wt.%), and Al-20wt.% Cu, Al-2wt.% Zr master alloys. In order to follow the structural evolution of Al_3Zr during heating, the ingot was solution heat treated (SHT) at 500 °C for three different durations, 20, 125 and 300 hours, all followed by water-quenching to room temperature. The SHT temperature and time are selected based on our previous works [27, 31]. Dark-field TEM (DF-TEM) characterization was conducted using a Thermo Fisher Tecnai G2 F20 TEM. HAADF-STEM imaging was achieved using a spherical aberration probe corrected Thermo Fisher Titan G2 60-300 microscope equipped with ChemiSTEM and operated at 300 kV. TEM thin foils were prepared by electropolishing using a twinjet polisher with 25% nitric acid solution in methanol at -25 °C. HAADF-STEM images were simulated using JEMS software [32] with parameters close to the experimental conditions.

2.2 Theoretical framework

First principles zero-temperature total energy calculations were performed using the projector augmented wave (PAW) method [33], as implemented in the Vienna *ab initio* simulation package (VASP) [34]. For the description of the exchange-correlation functional, the Perdew-Burke-Ernzerhof generalized gradient approximation [35] was employed. The Zr 4*p* semi-core states were added as valence states in the simulations. A plane wave cut-off energy of 325 eV and a *k*-point separation of 0.065 $Å^{-1}$ was found to ensure convergence at the meV/atom level for the computed formation energy (see Eq. (1)) differences. All calculations employed the 'Accurate' VASP setting and the Methfessel-Paxton scheme of order 2 [36] (smearing parameter 0.1 eV) for introduction of electronic state partial occupancies around ε_F. Convergence in the electronic self-consistency loop was defined by the energies in consecutive iteration steps differing by less than 10^{-5} eV, while the

criterion for the ionic self-consistency loop was that all force components on atoms in the simulation cell be within 0.01 eV/Å.

For the part involving bulk phase calculations, formation energies E_f (in eV/atom) were used to obtain stabilities:

$$E_f(N_{Al}, N_{Cu}, N_{Zr}) = E(N_{Al}, N_{Cu}, N_{Zr}) - (N_{Al}E_{Al} + N_{Cu}E_{Cu} + N_{Zr}E_{Zr})/(N_{Al} + N_{Cu} + N_{Zr}) \quad (1)$$

In this expression, N_X denotes the number of atoms with type X in the unit cell, while E_X and E correspond to the energy of X in its bulk phase and of the bulk precipitate, respectively. To further test the level of precision in calculations, comparison was made with energies of selected known Al-Cu-Zr alloy phases, Al_3Zr, Al_2Zr, Al_2Cu, and AlCu, as described in the Open Quantum Materials Database (OQMD) [37, 38]. For these phases, all formation energies were computed at the precision of the present work, and found to be within 2 meV/atom of the (highly precise) OQMD values.

For the simulations involving Cu agglomeration at a formally isolated extended defect in $L1_2$-$Al_{3-x}Cu_xZr$ $L1_2$, the Cu partitioning energy E_p was used as a measure for the preference of the reaction. E_p denotes the energy change when incorporating Cu from the environment and expelling a precipitate atom from its initial site in the local region where Cu agglomerates. For the generalized case where more than one Cu atom is moved into the precipitate, the mean partitioning energy $\langle E_p \rangle$ (in eV/Cu atom) is defined as:

$$\langle E_p(N_{Zr} + N_{Al}) \rangle = (E_{final} - E_{init} + N_{Zr}\mu_{Zr} + N_{Al}\mu_{Al} - (N_{Zr} + N_{Al})\mu_{Cu})/(N_{Zr} + N_{Al}) \quad (2)$$

Here, E_{init} and E_{final} denote the energies of the initial and final precipitate local regions respectively, while N_Y denotes the number of expelled precipitate atoms of type Y (Y = Al/Zr), and μ_X is the chemical potential of element X. In general, the expelled Zr atoms were viewed in the present work as relocating in the precipitate, as justified by the low solubility of Zr in Al. The Zr chemical potential was chosen as $\mu_{Zr} = Al_3Zr - 3\mu_{Al}$, with $\mu_{Al} = E_{Al}$, reflecting the local thermodynamic equilibrium experienced between precipitate and matrix when ignoring the Cu presence. Cu was

found to be most favorably included from the matrix, with μ_{Cu} obtained by placing a formally isolated Cu atom in an fcc Al supercell comprising 3×3×3 conventional unit cells, and subtracting the weighted energy of μ_{Al}; $\mu_{Cu} = E_{Al107Cu} - 107\mu_{Al}$.

Generally, computational studies involving {100} APB related defects presumed these to be isolated, fully adapting structurally to the surrounding $L1_2$-$Al_{3-x}Cu_xZr$ precipitate. In Sec. 4.3, this assumption implies that the chosen defect plane dimensions were those of $L1_2$-Al_3Zr throughout.

3. Results

3.1 Low magnification TEM imaging of the dispersoid particles

Fig. 1 shows DF-TEM images of the Al_3Zr dispersoids formed during SHT at 500 °C for 20 hours (Fig. 1(a, b)) and 125 hours (Fig. 1(c)), respectively. It should be noted that the eutectic Al_2Cu phase is completely dissolved during these SHT conditions; the above-mentioned dispersoids were the only precipitates observed in the system. Following heating for 20h, spherical Al_3Zr particles are homogeneously distributed with high density in the Al matrix. In some regions, the Al_3Zr particles are aligned in parallel rows as shown in Fig. 1(b). These dispersoids are most likely formed on dislocations due to the reduced strain energy barrier in such regions [13]. All Al_3Zr particles formed at this stage have an $L1_2$ structure as evidenced by the SAED pattern in Fig. 1(a, b). The location of the additional $L1_2$ superspots halfway towards the spots from the Al matrix confirm the "cube-on-cube" relationship between the $L1_2$ phase and the matrix. Some ellipsoidal $L1_2$-Al_3Zr particles exhibit defects in the form of sharp lines of no-contrast parallel to {100}-type planes inside the particles (marked by yellow arrows in Fig. 1(a,b)). Based on previous literature [9, 39], these defects can be identified as APBs originating from the transition of $L1_2$ to an imperfect $D0_{23}$, and hence represent the early stages of the $L1_2 \rightarrow D0_{23}$ transformation.

After heating at 500 °C for 125h (Fig. 1(c, d)), most of the Al_3Zr particles still

maintain the $L1_2$ structure, with a slight increase in particle size. Knipling et al. [9] reported that numerous disk-shaped, equilibrium $D0_{23}$-Al_3Zr phase particles have formed in Al-Zr alloys after heat treatment at 500 °C for 100h. In the Al-Cu-Zr alloy used in the present work, almost no $D0_{23}$ phase is observed at this stage, emphasizing the beneficial effect of Cu on the stability of the $L1_2$ phase. In addition to the spherical and ellipsoidal Al_3Zr particles, about 30% of the observed particles are plate-like, marked by the red arrows in Fig. 1(c, d). From the SAED pattern of Fig. 1(c), a rectangular arrangement of spots with an aspect ratio of 3 is observed (marked by a blue rectangle), which is different from that of the $L1_2$ and $D0_{23}$ structures. This observation indicates the formation of a new phase in the present Al-Cu-Zr alloy. Atomic-resolution HAADF-STEM experiments revealing the atomic structure of these plate-like particles are presented in Sec. 3.4.

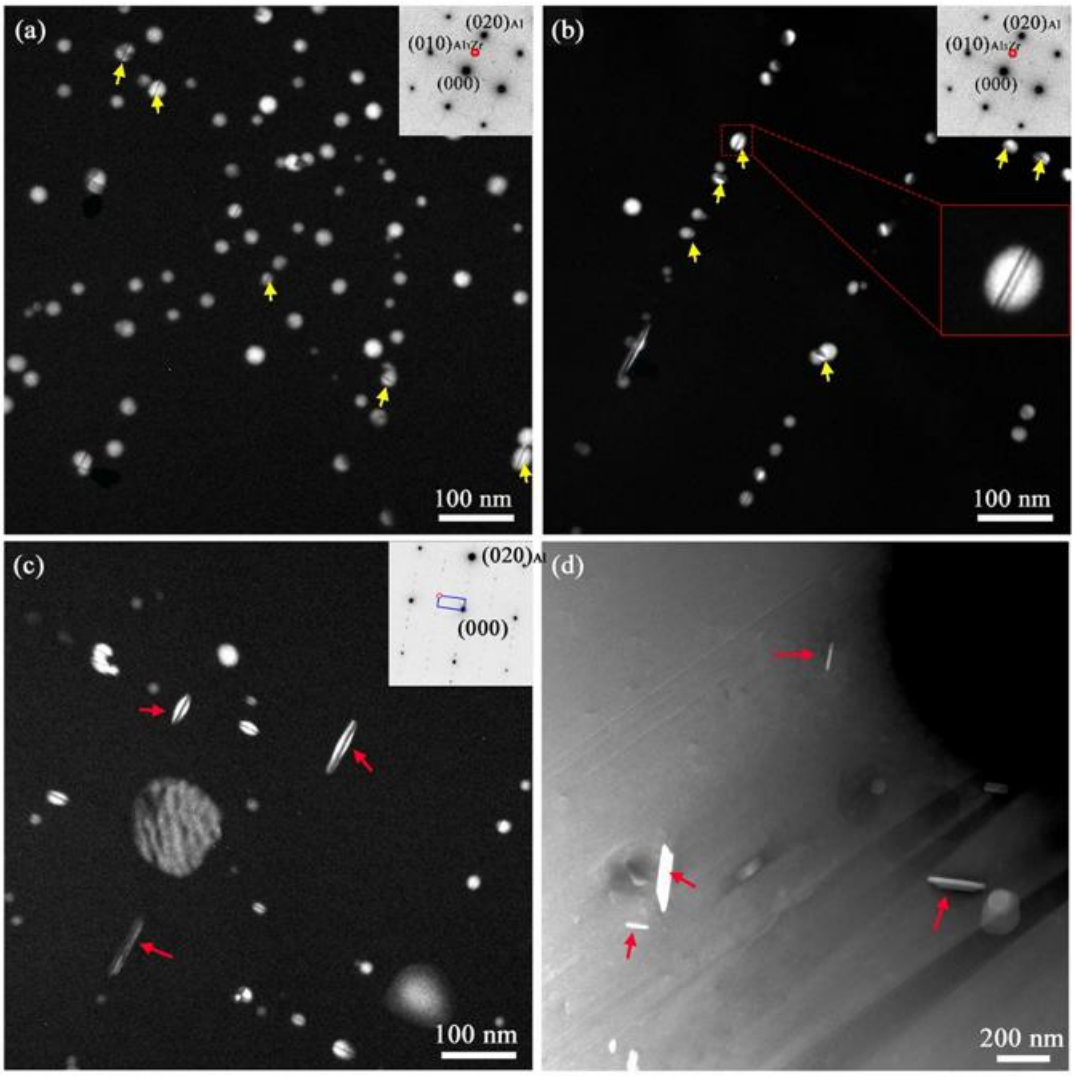

Fig. 1 DF-TEM images of the Al_3Zr particles formed during SHT at 500 °C for (a, b) 20 hours and (c) 125 hours, identified using the spot surrounded by red circles in the SAED patterns. (d) Low magnification HAADF-STEM image of the Al_3Zr particles formed during SHT at 500 °C for 125h. The presence of APBs within the Al_3Zr particles is marked by yellow arrows, while plate-like particles are marked by red arrows.

3.2 Atomic-scale characterization of the $L1_2$ phase and the $L1_2 \rightarrow D0_{23}$ transition

Fig. 2(a) shows an HAADF-STEM image of a spherical Al_3Zr particle formed after SHT at 500 °C for 20h, viewed along the $[001]_{Al}$ zone axis. An enlarged image of the Al_3Zr/Al-matrix interface is shown in Fig. 2(b). Here, the $L1_2$ phase can be

clearly identified. A good coherency between precipitate and matrix can also be observed in the same figure. The lattice parameter of the $L1_2$ phase and using the Al matrix as reference is measured as a = 4.02 Å, which is slightly smaller than the value of 4.08 Å reported in the literature [7]. Furthermore, the intensity line profile on the Al columns (Fig. 2(b, c)) shows that the intensities of Al columns in the $L1_2$ phase are higher than those of the Al matrix, indicating that some heavier solute atoms are incorporated in the $L1_2$ phase at the position of the Al atoms. Since the affinity of Cu for $L1_2$ has already been stressed in the literature [27- 30], these solute atoms are suspected to be Cu. EDX mappings of the $L1_2$ particle are shown in Fig. 2(d-f). As expected, a periodic square arrangement of Zr atoms can be clearly observed, i.e., this element is essentially confined to its own sublattice, supporting the scenario invoked above. The composition of the $L1_2$-Al_3Zr particle is measured as 62.1±3.6Al-13.4±2.1Cu-24.5±4.1Zr (at.%), based on the expected relation (Al+Cu)/Zr = 3 (full occupancy on each precipitate sublattice). This result suggests a stoichiometry of $Al_{2.5}Cu_{0.5}Zr$ for the $L1_2$ particles, in agreement with the earlier report by Hu et al. [30]. Since the measured Cu concentration significantly exceeds what may be explained by $L1_2$/Al interface decoration, it can be anticipated that the majority of the Cu atoms must be incorporated in the interior of the $L1_2$-Al_3Zr phase via partial substitution of the Al atoms as proposed. An $Al_{2.5}Cu_{0.5}Zr$ model, presuming randomly distributed Cu in the precipitate interior, is shown in Fig. S1. This model was used for the simulation of the HAADF-STEM contrast in Fig. 2(b) (yellow dotted rectangle). The simulated line profile of the Al columns (marked by a red line) is superposed upon the experimental data in Fig. 2(c). It shows a good agreement between simulation and experiment, which further consolidates the assumption of partial substitution of Al atoms by Cu in the $L1_2$ particle. Further investigations indicated that the particle examined in Fig. 2 is representative for this alloy condition. In particular, Cu-free $L1_2$ precipitates were not observed.

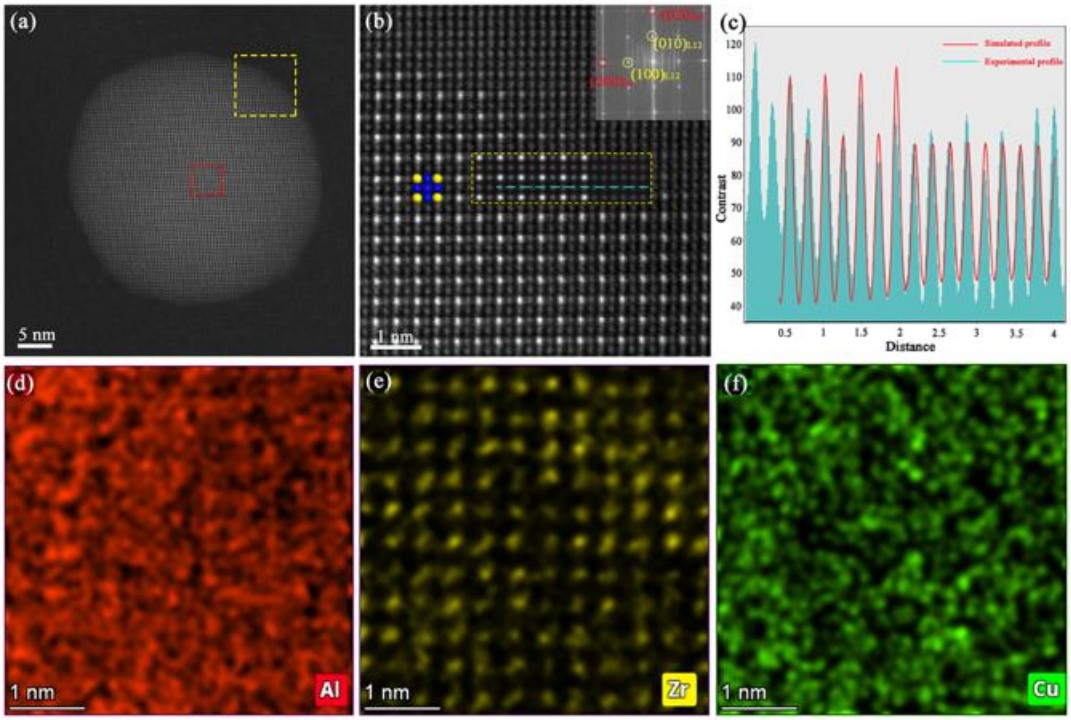

Fig. 2(a) HAADF-STEM image of an $L1_2$-Al_3Zr particle formed after SHT at 500 °C for 20h, viewed along the $[001]_{Al}$ zone axis. (b) Enlarged view of the Al_3Zr/Al-matrix interface (yellow dashed square in (a)). A unit cell with Zr and Al atoms marked by yellow and blue spheres, respectively, is indicated. A superimposed simulated HAADF-STEM image is delimited by a yellow dashed rectangle. (c) Experimental (green) and simulated (red) line profiles of the Al columns along the blue line in (b). (d-f) EDX mapping of Al, Cu and Zr in the interior of the $L1_2$ phase (red dashed square in (a)).

The HAADF-STEM image of Fig. 3(a) shows a set of isolated planar defects formed in the $L1_2$-Al_3Zr particle. In the enlarged view of the defect crossing the entire particle (Fig. 3(b)), the unit cells on both sides of the planar defect (red line) are shifted along this plane by *a*/2. This defect can thus be identified as a (010) APB formed by a shear of a/2[101] in the $(010)_{L12}$ plane. The {010} APBs in the $L1_2$ phase have been widely reported in the literature [4, 13, 27] and are considered as the onset of the transformation to $D0_{23}$. Fig. 3(c) presents a 'lens' shaped Al_3Zr particle exhibiting a sandwich structure. The outer regions exhibit the $L1_2$ structure, while the core region can be identified as $D0_{23}$ as shown in the enlarged image of Fig. 3(d). The

$D0_{23}$ phase is formed when APBs are introduced on every second $(010)_{Al}$ plane of the $L1_2$ phase. EDX mappings of the $D0_{23}$ phase are shown in Fig. 3(e-g). The $D0_{23}$ composition is measured as: 73.8±2.4 Al-22.2±2.3 Zr-3.35±0.48 Cu (at.%). The Cu concentration in the $D0_{23}$ phase is notably lower than what is observed for the $L1_2$ phase, suggesting that the $L1_2 \rightarrow D0_{23}$ transformation is associated with the expulsion of Cu atoms. Fig. 3(h-g) show the Cu mapping and corresponding line profile at the $L1_2/D0_{23}$ interface. It can be seen that Cu concentration drops as soon as the $D0_{23}$ phase region is entered, indicating that even isolated APBs may be capable of expelling Cu. The presence of such a 'Suzuki effect' (a solute redistribution in response to an extended defect introduction) could change the relative stability of the APB and hence have a significant influence on the understanding of the particle evolution. It also can be stressed that the APBs in Fig. 3(a) are favorable defects, as evidenced by the observation that the particle morphology (away from spherical) is linked to an increase in the APB area.

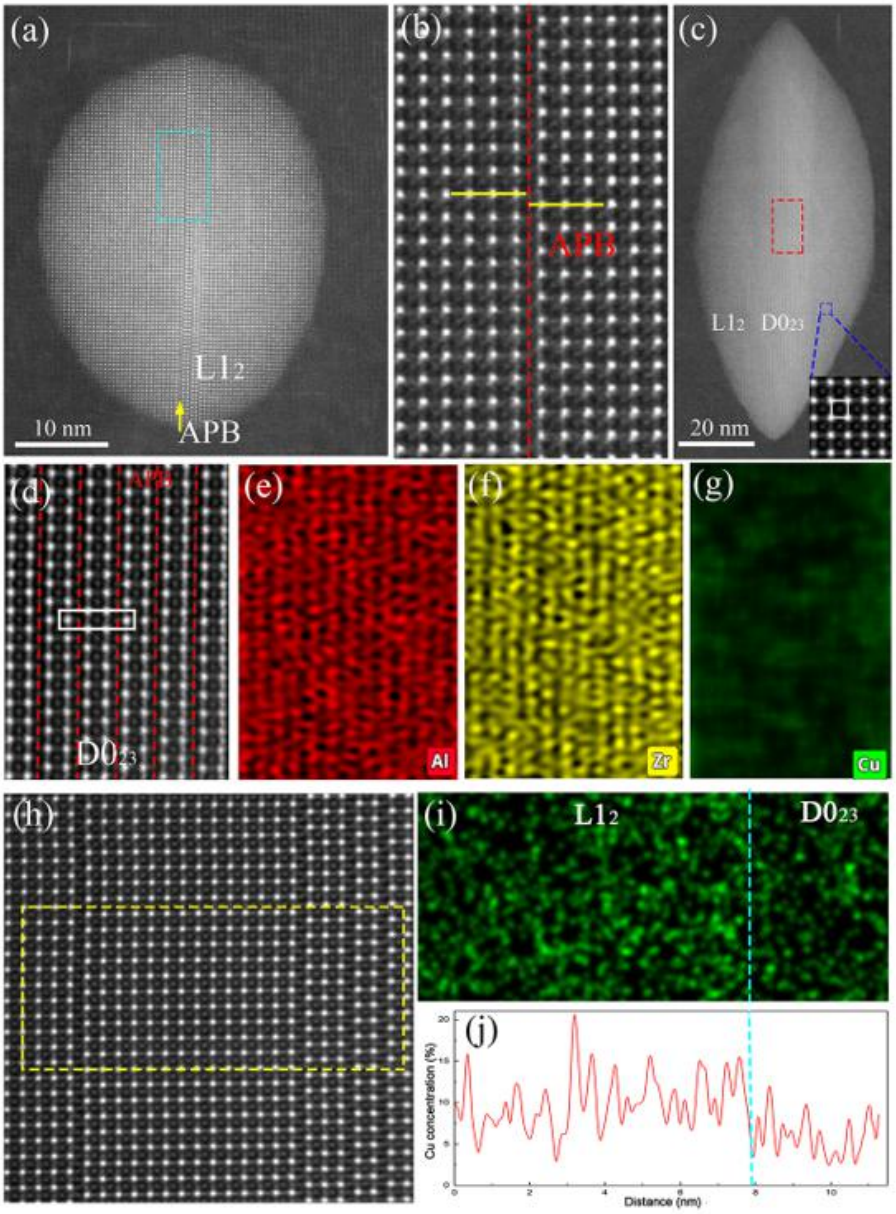

Fig. 3 (a) HAADF-STEM images of an $L1_2$-Al_3Zr particle with isolated APBs. (b) Enlarged image of the region marked by a blue dashed rectangle in (a). (c) HAADF-STEM image of a 'lens' shaped Al_3Zr particle. (d) Enlarged image showing the $D0_{23}$ phase in the core region (red dashed rectangle) of the particle in (c), (f-g) EDX mapping of the $D0_{23}$ phase in (d). (h) Enlarged image showing the $D0_{23}/L1_2$ interface for the particle in (c). (i, j) EDX mapping of the Cu content in the region of (h) marked by a yellow dashed rectangle. Unit cells are marked by white lines, and the APBs are marked by red dashed lines.

3.3 Segregation of Cu atoms at APBs

For some $L1_2$-Al_3Zr particles (about 10% of the total number of $L1_2$-Al_3Zr particles, see Fig. 4(a)), APB creation is found to induce a local atomic arrangement visibly different from the case of Fig. 3(a). Fig. 4(b) shows an enlarged image of the APB in Fig. 4(a), highlighting how an array of atomic columns with contrast lower than Zr but higher than Al is segregated on the Al-Zr layer adjacent to the APB. The EDX maps of Fig. 4(c-e) show that these segregated atomic columns are primarily Cu. A larger magnification of the Cu segregation region is presented in Fig. 4(f). From this image, it may be deduced that Cu segregation causes a local shrinkage of the unit cell along the APB plane normal. The distance between two Zr columns in the $L1_2$ structure (4.02 Å) is decreased to 3.8 Å for the case where Cu has substituted Zr in one column. The Cu layer is notably corrugated. Indeed, a periodic displacement of each Cu column that deviates from the cubic lattice of the $L1_2$ phase can be clearly observed. Each Cu column moves toward the nearest Zr column by 0.1 Å, probably reflecting an interaction between Cu and Zr. A schematic illustration of the Cu segregation adjacent to the APB plane in Fig. 4(f) and the corresponding simulated STEM image are shown in Fig. 4(g) and Fig. 4(h), respectively. A good agreement is noted between the simulated and experimental intensities, supporting the conclusion of a replacement of Al and Zr with Cu in the layer adjacent to the APB. To the best of the author's knowledge, direct atomic scale observation of segregation of Cu in a plane adjacent to the APB plane of the $L1_2$-Al_3Zr phase has not been reported previously in the literature.

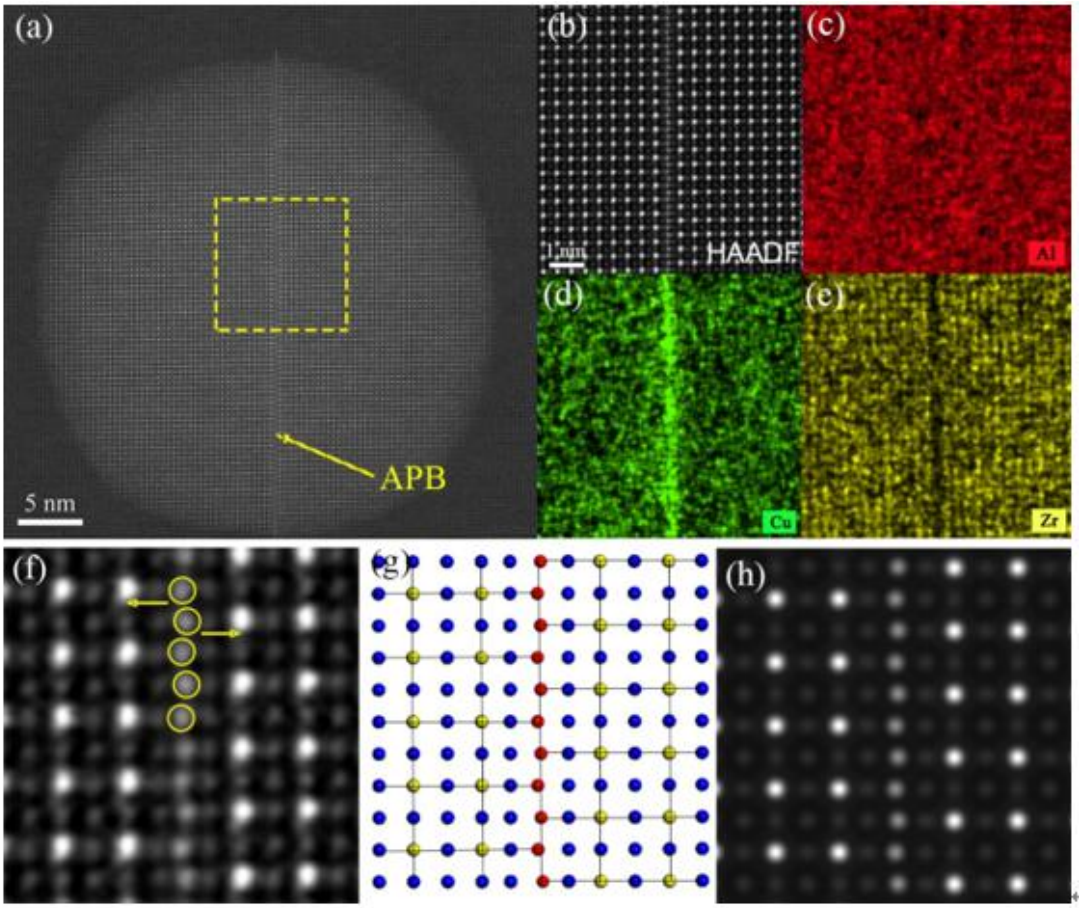

Fig. 4 (a) HAADF-STEM image of a spherical $L1_2$-Al_3Zr particle with a single APB after SHT at 500 °C for 20h. (b-e) Enlarged image (dashed yellow square in (a)) and corresponding EDX maps of the APB. (f) Enlarged image showing the segregation of Cu atoms in the plane adjacent to the APB plane. (g, h) Schematic illustration of the Cu segregation at the APB and a corresponding STEM image simulation. The Zr, Al and Cu atoms are marked by yellow, blue and red spheres, respectively.

Figures 5(a, b) show two ellipsoidal Al_3Zr particles with APBs. Enlarged images of the regions framed by blue dashed rectangles are shown in Fig. 5(c, e). In Fig. 5(c), the APB and the adjacent Cu layer (indicated by red and blue dotted lines, respectively) are coupled with an APB without Cu segregation (red dotted line). This observation indicates that APBs with and without Cu segregation can not only coexist, but also closely interact within one Al_3Zr particle at the early stage of $L1_2$ structural transformation. Due to the presence of two adjacent APBs, the second APB restores

the changes induced by the first APB. No shift can be observed for the $L1_2$ lattices outside the region delimited by the two APBs (black squares in Fig. 5(d)), indicating an "in-plane" relationship for the two $L1_2$ lattices separated by APBs. In Fig. 5(e), it can be seen that two APBs without Cu segregation (red dotted lines) enclose the Cu segregation layer (blue dotted line) in a symmetric arrangement. A schematic illustration of these APBs is presented in Fig. 5(f), where it can be seen that the two $L1_2$ lattices outside the region delimited by the outer APBs exhibit an "anti-phase" relationship with a shift of a/2[110] with respect to each other. This confirms that the combination of APBs with and without Cu segregation can result in the local formation of complex substructures different from $D0_{23}$.

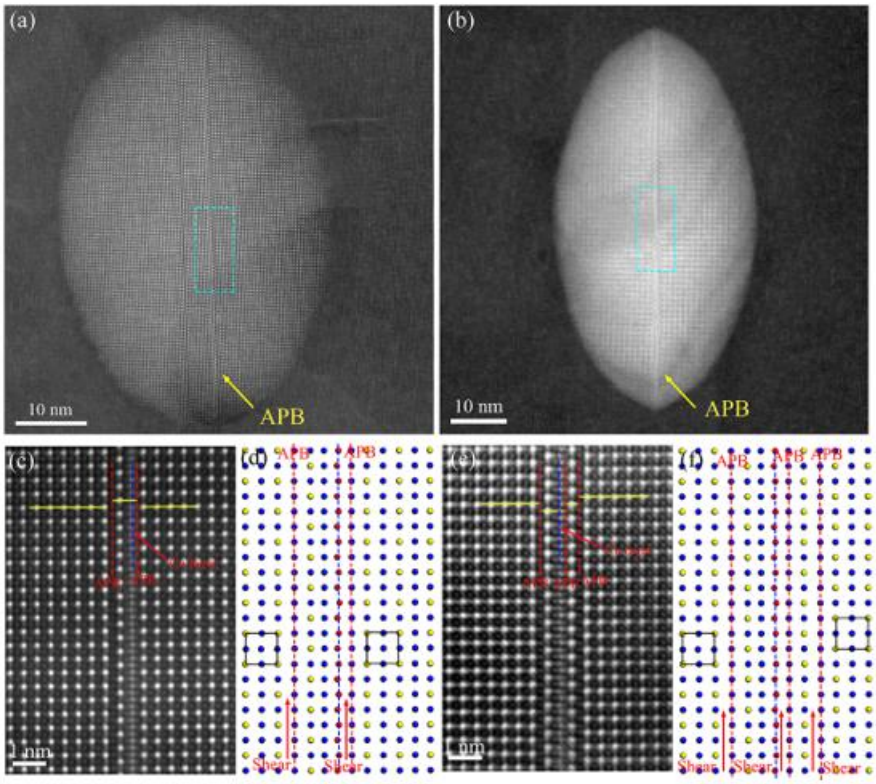

Fig.5 (a, b) HAADF-STEM images of two ellipsoid Al_3Zr particles with APBs after SHT at 500 °C for 20h. (c, e) Enlarged images of the regions framed by blue dashed rectangles are presented in (a) and (b). (d, f) Schematic illustration of the APBs in (c) and (e).

3.4 Formation of a new phase by periodic arrangement of Cu segregation layers

Upon heat treatment at 500 °C for 125h, a large number of plate-like particles (accounting for 40% of the total number of particles) are formed. Fig. 6(a) exhibits a low-magnification HAADF-STEM image of a plate-like particle viewed along a $<001>_{Al}$ zone axis. From the enlarged image in Fig. 6(b), Cu segregated layers can be seen to be periodically arranged. The convergent beam electron diffraction (CBED) pattern (Fig. 6(c)) shows a 4-fold rotational symmetry with two mirror planes at 45°, demonstrating that the new phase has a tetragonal structure with space group P4/nmm. Atomic resolution EDX mappings in Fig. 6(d-f) reveal that Cu and Zr occupy non-overlapping regions within the particle. In order to investigate the atomic structure of this new phase, HAADF-STEM images and corresponding FFT patterns were acquired along a $<110>_{Al}$ zone axis on another particle (Fig. 7(a, b)). The APBs are not visible along this viewing direction, as opposed to the segregated Cu layers. By analysis of the periodic arrangement of atomic columns along these different directions, the new tetragonal phase may be identified as Al_4CuZr with lattice parameters a = 11.8 Å and c = 4.04 Å. An atomic model of the Al_4CuZr phase is presented in the insert of Fig. 6(g), with the phase atomic coordinates included in Table 1. The good agreement between the experimental and simulated FFTs in Fig. 6(g) validates the proposed model. Schematic illustrations and simulated HAADF-STEM images of the Al_4CuZr phase viewed along its <100> and <110> zone axes are presented in Fig. 6(h, i) and Fig. 7(c, d), respectively. Both simulated images are in good agreement with the experimental ones. It may be concluded from this analysis that any structural and compositional deviations from the proposed phase will represent weak modulations only.

The composition Al_4CuZr is not linked to any known phase in the Al-Cu-Zr phase diagram. Fig. 6(a) thus represents the first experimental evidence of this new phase. It is an intriguing aspect of this phase formation that the coupling of APBs with and without nearby Cu segregation shown in Fig. 4(f) can now be identified as the creation of a sheet of Al_4CuZr unit cells. This observation indicates that the introduction of APBs in the $L1_2$ structure may trigger a transformation to either $D0_{23}$ or Al_4CuZr, depending on the Cu response to these APBs.

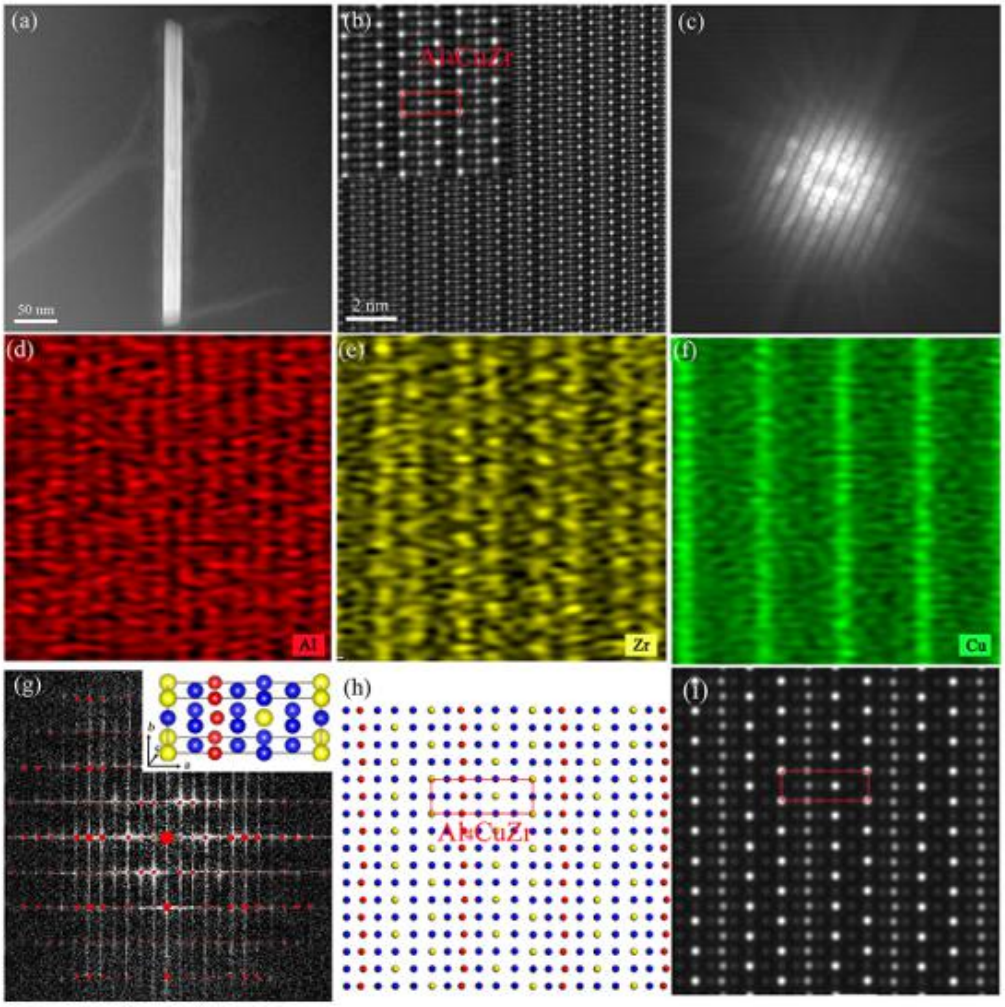

Fig. 6 (a) Low-magnification image of a plate-like particle (Al_4CuZr phase) formed after SHT at 500 °C for 125h, viewed along a $<001>_{Al}$ direction. (b) High resolution HAADF-STEM image of the particle in (a). (c) CBED pattern from the same particle. (d-f) Atomic-resolution EDX maps of the Al_4CuZr phase. (g) Experimental and simulated (red dots) FFT pattern of the Al_4CuZr phase. The atomic model of the phase is attached in the upper-right corner. (h, i) Schematic illustration and simulated HAADF-STEM image of the Al_4CuZr phase viewed along the [100] direction.

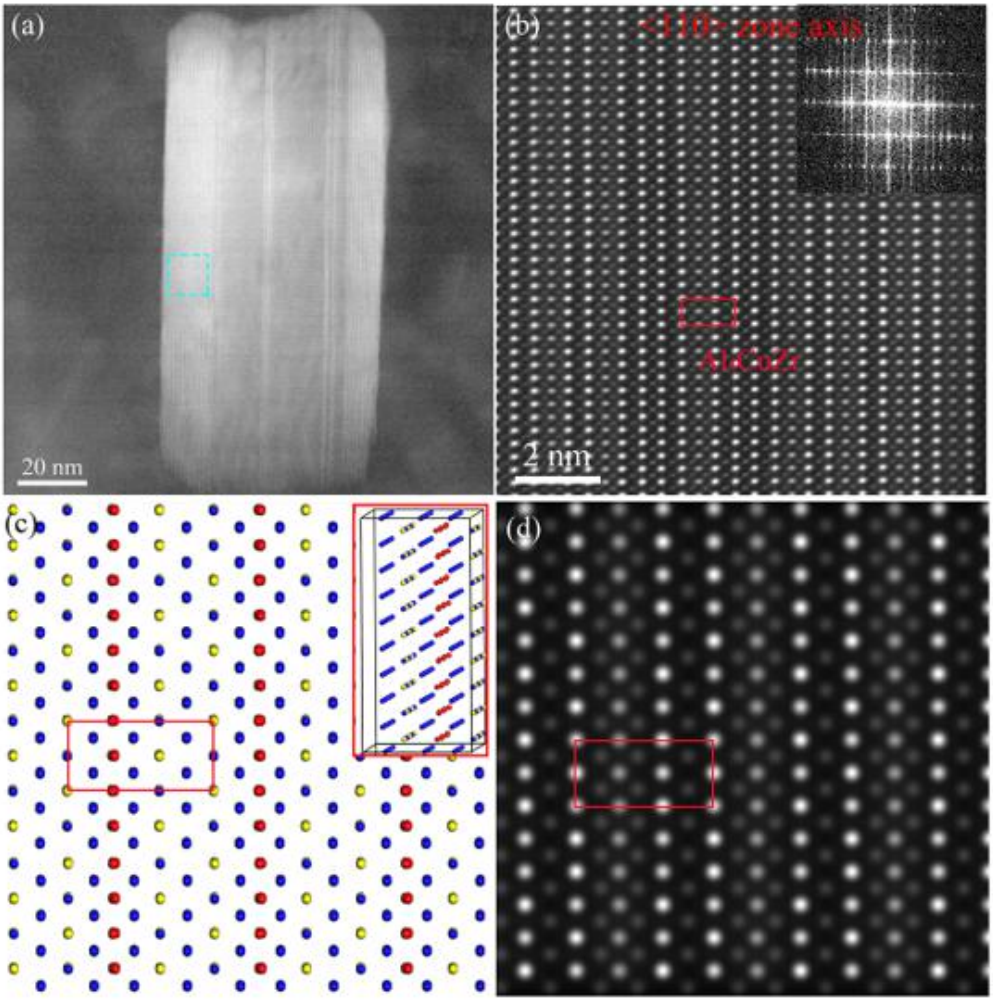

Fig. 7(a) Low-magnification image of a plate-like particle formed after SHT at 500 °C for 125h, viewed along a $<011>_{Al}$ direction. (b) High resolution HAADF-STEM image of the plate-like particle in (a). (c, d) Schematic illustration and simulated HAADF-STEM image of the Al_4CuZr phase viewed along its <011> direction. Note that each atom column in any of the vertical lines of columns with alternating Al and Zr in (c) has a mixing of Al, Zr (see inset in (c)).

Table 1 Atomic coordinates of the Al_4CuZr phase (cell dimensions a = 11.8 Å, c = 4.04 Å). See Fig. 6(g) for a visual presentation of the structure.

Atoms	X	Y	Z
Zr	0	0	0
Zr	0.629	0.5	0.5

Al	0	0.5	0.5
Al	0.177	0.5	0
Al	0.177	0	0.5
Al	0.451	0.5	0
Al	0.451	0	0.5
Al	0.629	0	0
Al	0.814	0.5	0
Al	0.814	0	0.5
Cu	0.306	0	0
Cu	0.322	0.5	0.5

3.5 Coexistence of post-$L1_2$ phases in a single particle

Fig. 8(a, b) show low-magnification HAADF-STEM images of two plate-like particles confining planar defects. Fig. 8(c, d) exhibit enlarged images of the regions framed by blue dashed rectangles in Fig. 8(a, b). Both particles are found to exhibit a composite structure involving unit cells of up to three different phases. In Fig. 8(c), it can be seen that the $L1_2$ phase coexists with the $D0_{23}$ phase in the left side. In the middle region, isolated Cu layers or Cu layer pairs (forming the Al_4CuZr phase with one/two-unit cell thickness) are embedded in $D0_{23}$. Finally, the right side is occupied by Al_4CuZr cells with a periodic arrangement of the Cu layers. In Fig. 8(d), the structure of the precipitate alternates between the $D0_{23}$ and Al_4CuZr phase. This result emphasizes that a structural transformation from $L1_2$ to both $D0_{23}$ and Al_4CuZr is possible within a single precipitate. The $D0_{23}/Al_4CuZr$ misfit is within 1% along the vertical direction in Fig. 8 (for $D0_{23}$-Al_3Zr lattice parameters, see, e.g., [3]), allowing for an essentially defect-free interface.

Fig. 9(a) shows a low-magnification HAADF-STEM image of a plate-like particle containing $D0_{23}$ and Al_4CuZr phases, which captures the $D0_{23}/Al_4CuZr$ interface perpendicular to the plate plane, i.e., terminating Cu layers in the precipitate. In Fig. 9(b), a single Cu layer is terminated within the $D0_{23}$ phase (marked by a red arrow). This Cu layer local environment is identical to Fig. 4(f), but as the layer

terminates, the environment on the right side is altered too, all APBs effectively moving one Al layer to the right, ensuring a defect-free $D0_{23}$ phase in the top part of the figure. In the region marked by a green arrow, Al_4CuZr unit cells formed by three Cu segregation layers are terminating, with a defect-free $D0_{23}$ phase appearing beyond this point. An IFFT image with the (010) reflection together with the corresponding local GPA map is shown in Fig. 9(c). In this figure, an interfacial dislocation can be clearly seen at the (010) $D0_{23}/Al_4CuZr$ interface marked by a green arrow in Fig. 9(b). An enlarged image of this region is shown in Fig. 9(d). In this figure, it can be seen that the introduction of a Cu segregation layer causes the surrounding layers to move considerably closer, similar to the situation for a lone Cu decorated APB in $L1_2$ as discussed in Sec. 3.3. Upon Cu introduction, the distance $2d_{Zr}$ between adjacent Zr columns on either side of the Cu-hosting layer is decreasing from 8.2 Å to 7.6 Å. For the (010) $D0_{23}/Al_4CuZr$ interface shown by the green arrow in Fig. 9(b), this lattice shrinkage leads to the formation of an interfacial dislocation. The lattice misfit along the plate normal, i.e., along the horizontal direction in Fig. 9(d), is measured as: $\delta = |d(100)_{D023}-d(100)_{Al4CuZr}|/d(100)_{D023}=|17.28-11.8|/17.28 = 31.7\%$, suggesting that an incoherent interface is formed. Altogether, the results shown in Fig. 9 suggest that dislocations play a role in mediating the transition between $D0_{23}$ and Al_4CuZr in the direction normal to the plate axis, regardless of the spatial dimensions of the Al_4CuZr region.

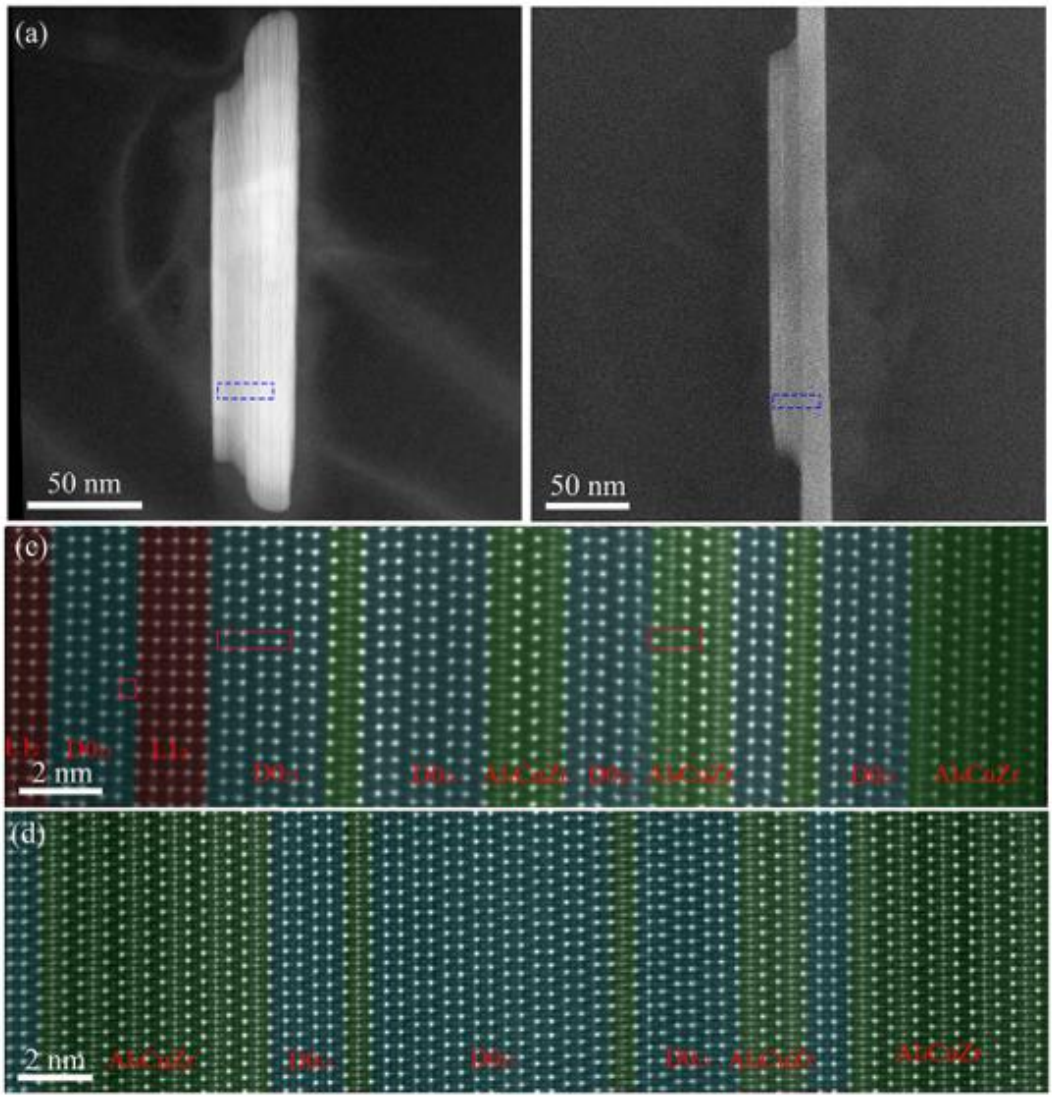

Fig. 8 (a, b) Low-magnification images of two plate-like particles, formed after SHT at 500 °C for 125h, hosting extended regions of more than one phase. (c, d) HAADF-STEM images of the regions delimited by blue dashed squares in (a, b). Different phases are highlighted in color.

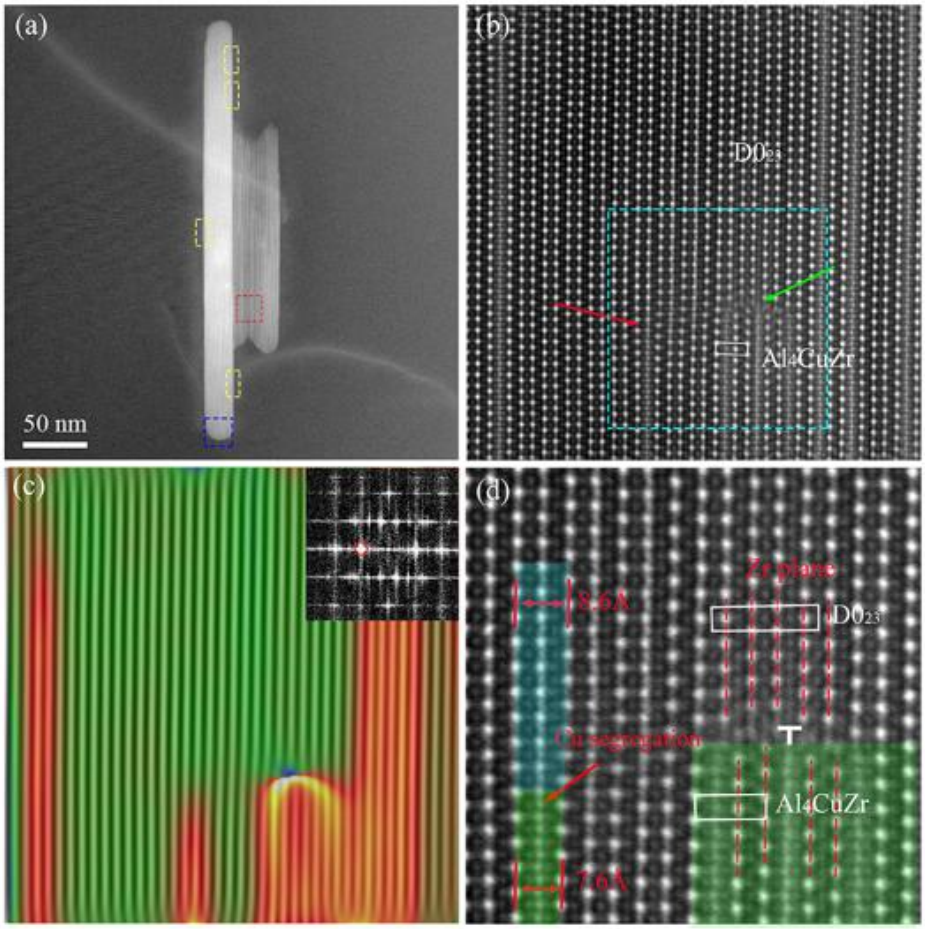

Fig. 9 (a) Low-magnification image of a plate-like phase hosting both $D0_{23}$ and Al_4CuZr, formed after SHT at 500 °C for 125h. (b) HAADF-STEM image of the (010) $D0_{23}/Al_4CuZr$ interface. (c) Overlapping of (100) IFFT image with the corresponding local GPA map. (d) Enlarged image of the region marked by the blue dashed square in (b).

In order to unravel the growth mechanism of the Al_4CuZr phase, enlarged images at the tip and lateral sides of the particle in Fig. 9(a) (marked by blue and yellow dashed rectangles, respectively) are shown in Fig. 10. At the tip of the Al_4CuZr phase (Fig. 10(a)), the Al_4CuZr/Al interface exhibits a curved morphology. In the enlarged image shown in Fig. 10(b), the Cu segregation layers of the Al_4CuZr phase are seen to penetrate into the Al matrix, indicating a high growth rate of these layers. The Al/Al_4CuZr lattice misfit along the (100) plane is calculated as: $\delta = | d(100)_{Al4CuZr} - 6d(100)_{Al} |/6d(100)_{Al} = |11.8-12.12|/12.12 = 2.6\%$. This result suggests that the

Al_4CuZr phase is coherent with the Al matrix along this plane, which is further confirmed by the IFFT image insert in the right corner of Fig. 10(b). By contrast, the calculated Al/$D0_{23}$ lattice misfit is: $\delta = | d(100)_{D023} - 8d(100)_{Al} |/8d(100)_{Al} = |17.28-16.16|/16.16 = 6.9\%$, suggesting that the $D0_{23}$ phase exhibits a semi-coherent interface with the Al matrix along the (100) plane. It follows that, unlike $D0_{23}$, the Al_4CuZr phase retains coherency with Al along all three directions, the precipitate-matrix misfit along the plate plane directions being quite small.

The low-magnification image of Fig. 9(a) suggests that the (010) habit plane is rather smooth, with no ledges. However, from the atomic-resolution HAADF-STEM images shown in Fig. 10(c-f), a few steps with a height of two $(100)_{Al}$ planes are visible (highlighted by yellow arrows). As shown at the bottom of Fig. 10(c), the (100) Al_4CuZr/Al interface may terminate in an Al-Zr layer, with the sequence of Al-Zr and Cu layers obeyed in bulk Al_4CuZr being retained all the way to the interface. Moving toward the top of this figure, however, an array of Cu columns showing a deviation from this sequence is found to segregate at the interface, at the 'expected' position of the next Al-Zr layer. At the bottom of Fig. 10(d), compared to the interface at the top of Fig. 10(c), an Al-Zr layer has been added at a separation of two $(100)_{Al}$ planes from the Cu layer. When moving toward the top of Fig. 10(d), yet an Al-Zr layer begins to be added at the same separation from the interface, but in addition, a swapping process is initiated for the Cu and Al-Zr layers behind this new layer, leading to the Al_4CuZr layer sequence being reestablished. The interface configuration at the top of Fig. 10(d) is thus identical to the configuration at the bottom of Fig. 10(c). Fig. 10(e, f) show how the (100) Al_4CuZr/Al interface may evolve differently. At the top of Fig. 10(e), the outermost three solute layers, each separated by two $(100)_{Al}$ planes, are all Al-Zr layers. However, at the bottom of Fig. 10(f), the normal Al_4CuZr layer sequence has again been reinstated via addition of Al-Zr layer at a separation of two $(100)_{Al}$ planes, and substitution of Cu in the last Al-Zr layer. The ledge height in Fig. 10(e) is twice that of Fig. 10(c), but the resemblance of the interface termination here to the $L1_2$ phase might nonetheless indicate easier nucleation. These results indicate that the lateral thickening of the Al_4CuZr phase is comparatively limited, probably

caused by a high barrier to ledge nucleation. The Al_4CuZr/Al lattice misfit along the 100 plane is measured as: $\delta = | d(010)_{Al4CuZr} - 2d(010)_{Al} |/2d(010)_{Al} = |4.04-4.04|/4.04 < 0.1\%$, explaining the good coherency of this interface.

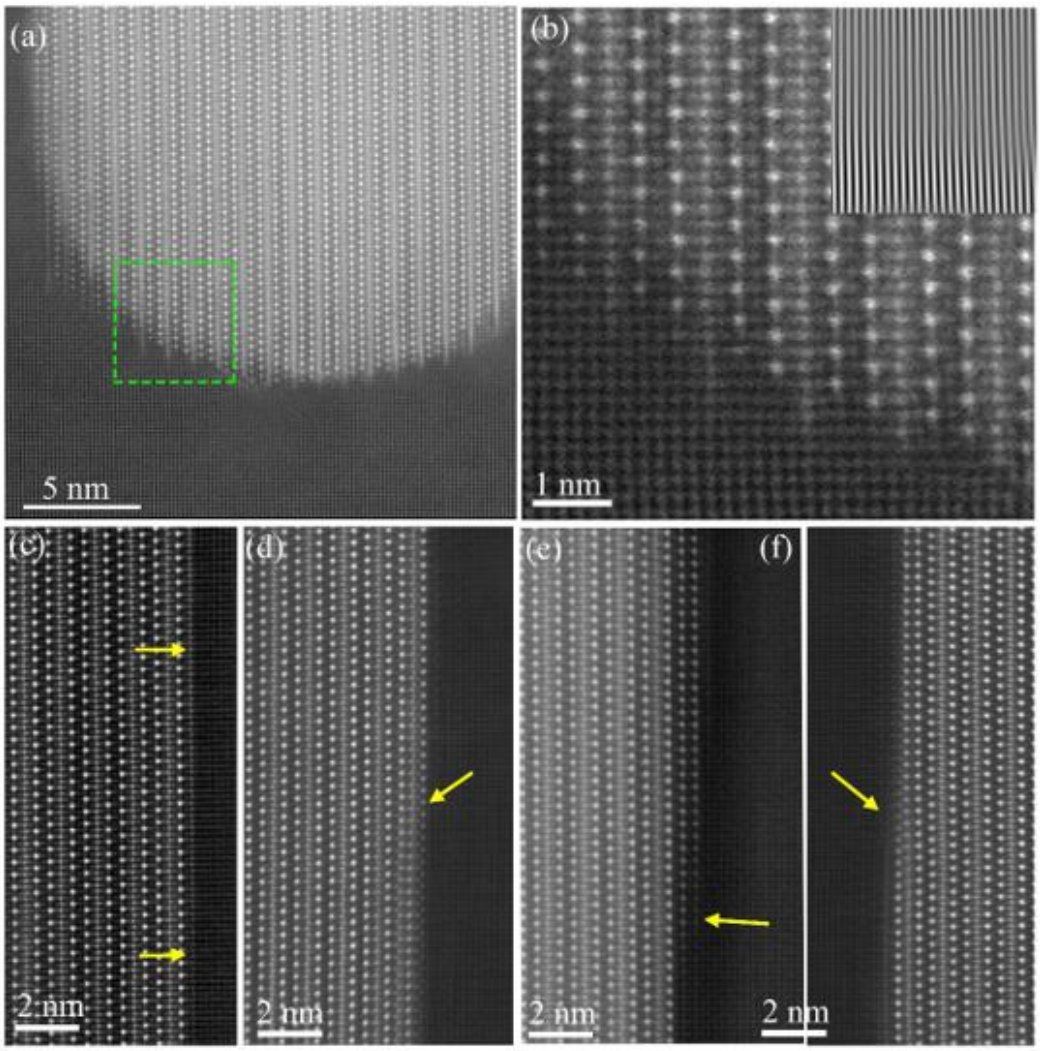

Fig. 10 (a) HAADF-STEM image at the tip of the Al_4CuZr phase presented in Fig. 9(a) (marked by blue rectangle). (b) Magnified image of the region marked by a green dashed square in (a). (c-f) HAADF-STEM image of the lateral sides of the Al_4CuZr phase presented in Fig. 9(a) (marked by yellow rectangles).

3.6. Dispersoid microstructure evolution upon long-term heating

To study the transformation path between the Al_4CuZr and $D0_{23}$ phases, the alloy was long-term heated at 500 °C for 300h. Fig. 11(a) shows a low-magnification image

of the dispersoids formed in this condition. It is clear that the dispersoids exhibit two different morphologies when viewed in this projection: rod-like and (roughly) rectangular. From the STEM-EDX maps of the two particles shown in Fig. 11(b-d) and Fig. 11(e-g), both can be identified as the Al_4CuZr phase. The respective compositions are measured as: 72.9±5.6 Al-11.9±4.8 Cu-15.2±5.4 Zr (at.%), and 71.4±5.6 Al-12.3±3.2 Cu-16.3±4.6 Zr, while the atomic-resolution HAADF-STEM image inserted in the right corner of Fig. 11(b) reveals the Al_4CuZr unit cell. The rod-like and rectangular particles are actually the plate-like Al_4CuZr phase viewed perpendicular to and along the plate normal, respectively. It is therefore concluded that all dispersoids transform to the Al_4CuZr phase after long-term heating at 500 °C.

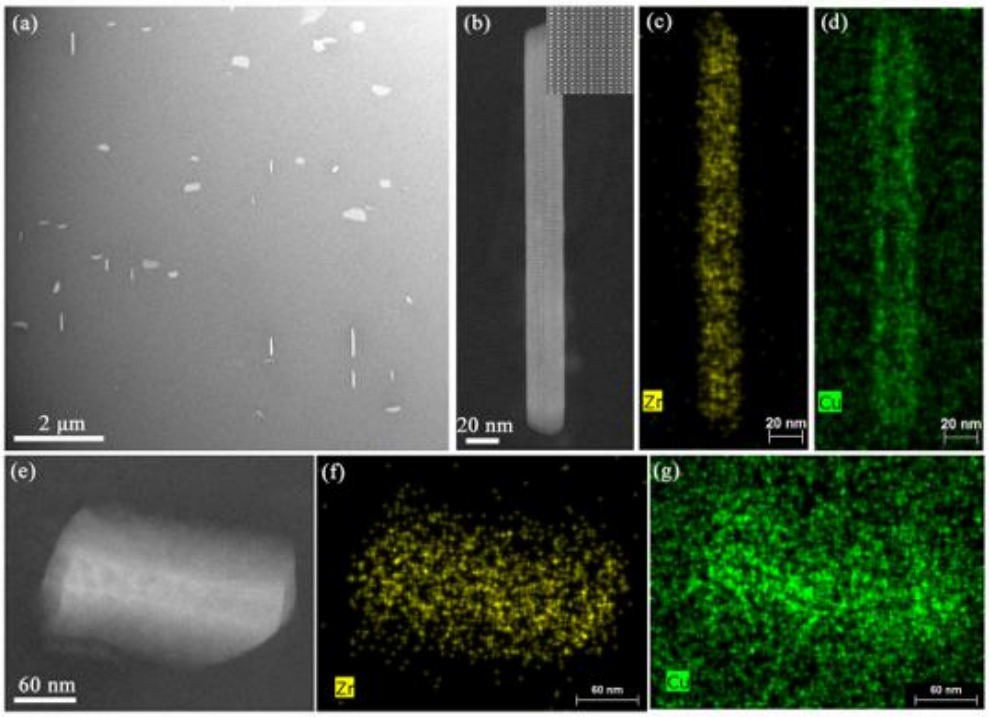

Fig. 11(a) Low-magnification image of the dispersoids formed after long-term heating at 500 °C for 300h. (b-d) HAADF-STEM image and corresponding EDX mapping of a selected rod particle, (e-g) HAADF-STEM image and corresponding EDX mapping of a selected rectangular particle.

4. DFT Calculations

4.1 Incorporation of Cu in the $L1_2$-Al_3Zr phase

Previous theoretical studies have predicted Cu incorporation on the Al sublattice

in the $L1_2$-Al_3Zr phase for an alloy with a Cu content at the level of this work [28]. The present studies have employed a cluster expansion (CE) algorithm (for details, see Supplementary Materials) to clarify the Cu distribution in the precipitate as a starting point for DFT investigation. A clear Cu-Cu repulsion was suggested in these studies, with an example of a typical $Al_{3-x}Cu_xZr$ cell shown in Fig. 12(a). Fig 12(b) shows part of the Al-Cu-Zr phase diagram at the experimental heating condition, with formation energy (out of the paper plane) plotted against alloy composition (point on the plane). The $Al_{3-x}Cu_xZr$ phase stability is determined by comparing a given configuration energy with the energy of the phase diagram tie-plane at the associated composition [40]. These tie-planes are energy plane triangular segments that host known phases at their corners. Compared to any alternative set of energy planes that may be constructed from linking the full set of known phase formation energies in this manner, the tie-planes produce the lowest energy at any chosen composition. A new phase with a formation energy that falls below the tie-plane energy represents a stable phase in the diagram and will alter the surrounding tie-plane(s). Conventionally, such a phase would be referred to as residing on the (lowest energy) convex hull of the Al-Cu-Zr alloy system.

As noted in Sec. 3.1, only the Al_3Zr dispersoids are observed following heating at 500 °C, for which reason all Al-Cu phases are excluded from the phase diagram in Fig. 12(b). The tie-plane, with which the $Al_{3-x}Cu_xZr$ energies should be compared, links Al_3Zr, Al_2Zr, and Cu. At the point of potential Cu incorporation in Al_3Zr, this phase adopts the $L1_2$ structure, for which reason the tie-plane connected with $L1_2$-Al_3Zr is discussed here. As shown in Fig. 12(c), the $Al_{3-x}Cu_xZr$ E_f values always fall below this tie-plane, suggesting the presence of an $L1_2$-$Al_{3-x}Cu_xZr$ phase on the convex hull. For the alloy system of the present work, this phase however is of relevance only if it modifies the preceding Al-Cu-Zr phase diagram through the creation of an ($L1_2$-$Al_{3-x}Cu_xZr$)-Al tie-line. Only in this case will the $L1_2$-$Al_{3-x}Cu_xZr$ phase represent a corner of the tie-plane linked to the alloy composition, indicating phase stabilization in the system under investigation. Due to the Cu-Cu repulsion in $L1_2$-Al_3Zr, emphasized by the convex formation energy curve in Fig. 12(c), an upper

limit to the Cu incorporation in the precipitate will be present. If x_0 defines the value of the Cu concentration ($C_{Cu,\ Al3Zr}$) at which the $L1_2$-$Al_{3-x}Cu_xZr$ formation energy attains its minimum in Fig. 12(c), any configuration with $x > x_0$ will fail to possess a tie-line with Al, because such a line does not cross the ($L1_2$-$Al_{3-x0}Cu_{x0}Zr$)-Cu tie-line favorably, and hence cannot be a tie-line. The energy curve in Fig. 12(c) cannot be accurately determined with the present methodology as the configurational entropy term is not well known. However, since Cu-Cu repulsion should significantly reduce the influence of this term for any appreciable Cu incorporation, the minimum in Fig. 12(c), $C_{Cu,\ Al3Zr} \approx 13\%$, is considered a fair estimate. This value is in good agreement with the observations (see Sec. 3.2). Further, both theory and experiment suggest that the updated Al-Cu-Zr phase diagram excludes the Cu-free dispersoid. The theoretical $Al_{3-x}Cu_xZr$ lattice parameter is found to vary roughly linearly over the range of relevant $C_{Cu,\ Al3Zr}$ values: $4.109 - 0.249*C_{Cu,\ Al3Zr}$ Å (see Fig. 12(d)). In the remaining theoretical discussions, the $L1_2$-$Al_{71}Cu_{10}Zr_{27}$ configuration ($C_{Cu,\ Al3Zr} = 12.3\%$) will be employed as an approximation to the experimentally reported dispersoid. The predicted $L1_2$-$Al_{3-x}Cu_xZr$ lattice parameter of 4.077 Å for this configuration is somewhat above the observed value of 4.02 Å, owing in part to theory overshooting the Cu-free cell dimension by 0.03 Å.

Table 2 Calculated formation energies (in eV/atom) of selected phases and configurations, known and proposed, from the Al-Cu-Zr phase diagram. For the $L1_2$-$Al_{3-x}Cu_xZr$ configurations, the zero-temperature formation energies have been tabulated (no entropy term).

Phase	E_f / eV/atom
$L1_2$-Al_3Zr	-0.4606
$D0_{23}$-Al_3Zr	-0.4880
Al_2Zr	-0.5398
$L1_2$-$Al_{77}Cu_4Zr_{27}$	-0.4743
$L1_2$-$Al_{75}Cu_6Zr_{27}$	-0.4804

$L1_2$-$Al_{71}Cu_{10}Zr_{27}$	-0.4900
$L1_2$-$Al_{67}Cu_{14}Zr_{27}$	-0.4850
Al_4CuZr	-0.4031

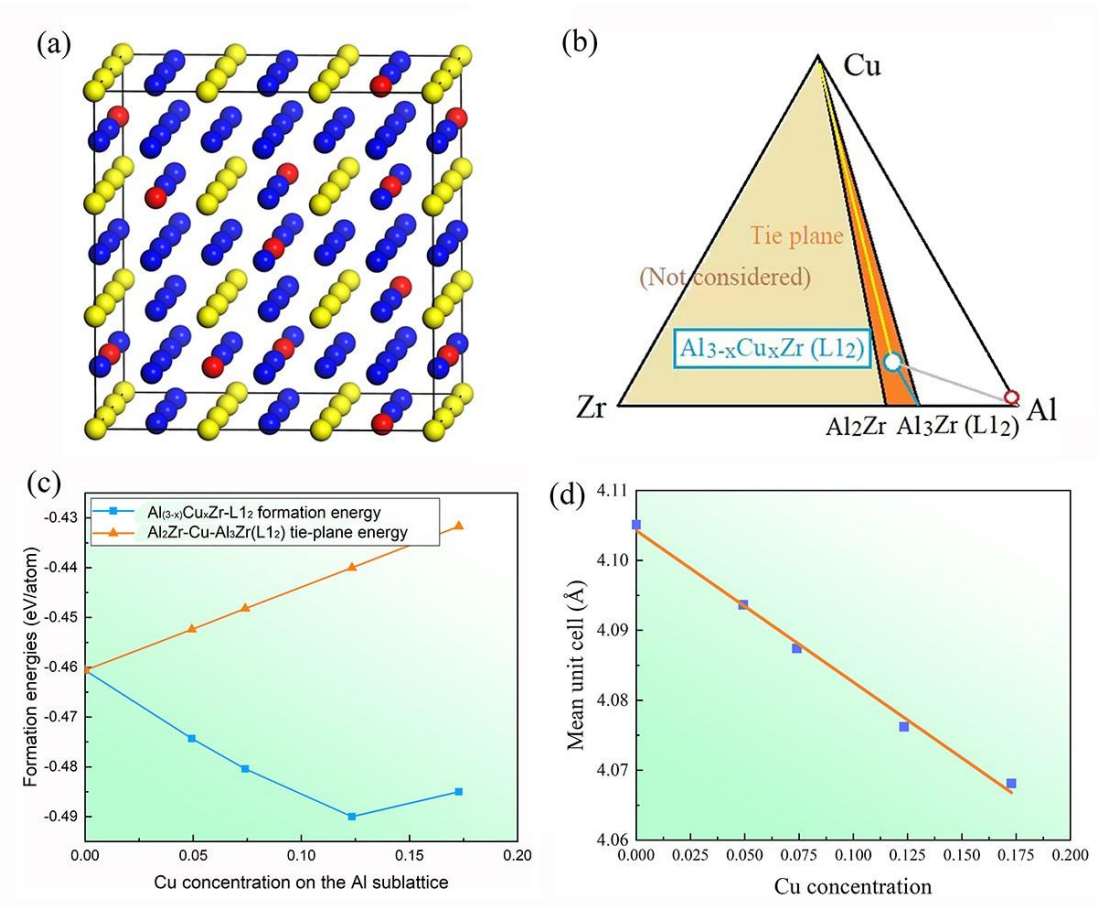

Fig. 12 (a) Schematic illustration of a $L1_2$-$Al_{3-x}Cu_xZr$ simulation cell (composition $Al_{75}Cu_6Zr_{27}$). Al, Zr, and Cu atoms are labeled with dark blue, yellow and red spheres, respectively. (b) Location of $L1_2$-$Al_{3-x}Cu_xZr$ configurations in the Al-Cu-Zr phase diagram at the experimental condition (heating at 500 °C). The yellow and grey lines are tie-lines between $Al_{3-x}Cu_xZr$ and, respectively, Cu and Al. The blue circle marks the estimated upper limit (≈ 13%) to Cu incorporation in $L1_2$, above which the $Al_{3-x}Cu_xZr$-Al tie-line vanishes, while the red circle marks the experimental alloy composition. (c) Calculated formation and tie-plane energies along the blue line in (b). (d) Theoretical lattice parameter of $L1_2$-$Al_{3-x}Cu_xZr$ (orange line: guide to the eye).

4.2 Creation of an APB with no Cu decoration in $L1_2$-$Al_{3-x}Cu_xZr$

For the simulations of extended {100} APB related defects in the $L1_2$-$Al_{3-x}Cu_xZr$ phase, cells with a defect separation of three conventional $L1_2$ unit cells were used, with an example shown in Fig. 13(a). In the absence of Cu, APB energy barrier calculations involved a cell dimension relaxation along the defect plane normal only (formally isolated APB), and force component optimization exclusively along the same direction for all intermediate configurations (γ-surface calculation). For Cu-hosting systems, all cell dimensions were additionally scaled in accordance with Fig. 12(d). Computed {100} APB energy barriers for selected $Al_{3-x}Cu_xZr$ configurations are shown in Fig. 13(b), while Fig. 13(c) displays the predicted variation of the barrier height and the APB-hosting configuration stability relative to the defect-free structure as a function of $C_{Cu,\ Al3Zr}$. Both energies are essentially linearly increasing. At $C_{Cu,\ Al3Zr}$ ≥ 4%, the APB is an energetically unfavored defect. At this transition point, the APB energy barrier height, or unstable stacking fault (USF) energy, has increased by roughly 130 mJ/m^2 from an initial value of 770 mJ/m^2. For the $Al_{71}Cu_{10}Zr_{27}$ configuration, APB creation is associated with an energy barrier roughly 50% above the value in Cu-free $L1_2$-Al_3Zr, suggesting Cu is effective in suppressing the activation of APBs, thereby stabilizing the $L1_2$ structure. These trends display qualitative agreement with earlier, less extensive studies [29, 30]. It is noted that the influence of Cu is chemical rather than structural: if Cu atoms were removed from the dispersoid but with the Cu cell dimension influence retained, a (weak) lowering of the APB energy barrier would be obtained.

The calculations of Fig. 13(b, c) do not take into account the possibility of any Suzuki effect upon APB creation. Experiment, however, suggests (see Fig. 3(a)) that the isolated APB in the Cu-hosting $L1_2$ phase observed in connection with the onset of the $L1_2 \rightarrow D0_{23}$ transition is a favorable defect, as evidenced by the notable relative growth of the APB plane when the particle morphology changes from spherical to elongated. This result is at odds with Fig. 13(c); since the experimentally reported value of $C_{Cu,\ Al3Zr}$ is well above 4%, an unfavorable APB should result. A likely explanation for this discrepancy, potentially supported by the experimental results in Sec. 3.2, is that Cu redistributes following the APB creation. Fig. 13(d) shows how a

formally isolated Cu atom in the $L1_2$ phase is strongly repelled by the APB plane. Since Cu is obviously mobile at the aging temperatures under consideration, the result suggests that the APB creation in Fig. 3 is too fast for any Cu redistribution to occur, but with this process (Fig. 13(c)) subsequently being accompanied by Cu depletion at the vicinity of the APB plane, resulting in a significant lowering of the initial defect energy. The implications of this finding are discussed further in Sec. 5.2. Additional experimental support for a significant Suzuki effect has been obtained from the EDX mapping of Fig. 3 which demonstrated that the $D0_{23}$ phase, characterized by a high density of APBs, has a low Cu concentration compared with $L1_2$.

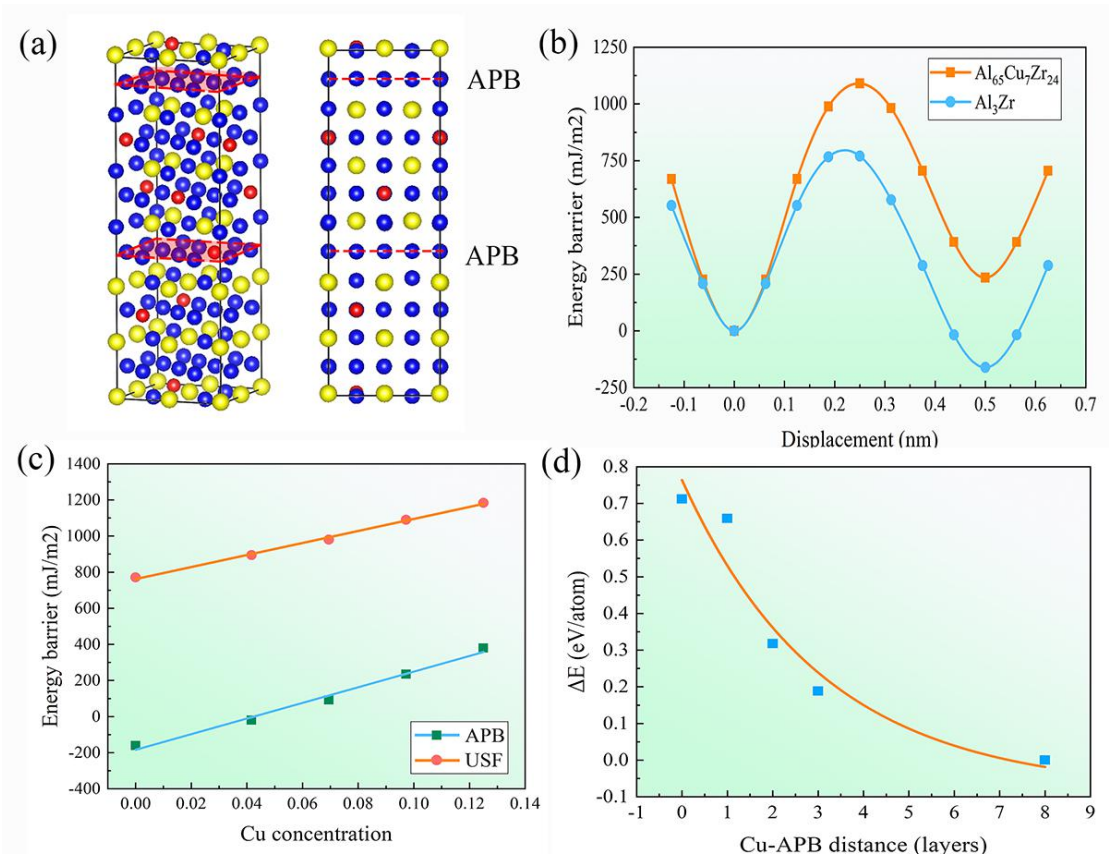

Fig. 13 (a) Schematic illustration of a simulation cell used for modelling the {100} APB energy barrier in $Al_{3-x}Cu_xZr$ (composition $Al_{65}Cu_7Zr_{24}$, APB fully created). The two defect planes in the cell have been highlighted in red. (b) APB energy barrier curves for two $L1_2$-$Al_{3-x}Cu_xZr$ systems. (c) APB energy barrier height (orange) and

APB defected configuration stability (blue) relative to the defect-free configuration, as a function of $C_{Cu,\ Al3Zr}$. (d) Energy of an isolated Cu atom at an APB in $L1_2$-Al_3Zr as a function of APB-Cu separation, relative to Cu in a bulk precipitate (highest x-coordinate).

4.3 Creation of a Cu-decorated APB in $L1_2$-$Al_{3-x}Cu_xZr$

The experimental results of Fig. 4 are surprising in two respects: (i) contrasting the conclusions of Sec, 3.2, 4.2, Cu is *attracted* to the {100} APB and (ii) the resulting Cu decoration is asymmetric, involving only one Al-Zr plane adjacent to the APB plane. The isolated APB in $L1_2$-Al_3Zr is a symmetric extended defect that would seem unable to trigger this asymmetry. However, during the theoretical APB creation (Fig. 13(b)), symmetry is broken, because the Al atoms of the ultimate APB plane stay 'locked' to one of the adjacent Al-Zr planes. Motivated by this observation, the theoretical investigations of the Cu decoration phenomenon of Fig. 4 have followed two paths. In the first scenario, the APB has been created at the outset, and in the second, the process is only 'halfway' complete, i.e., the extended defect simulated is the USF configuration (example shown in Fig. 14(a)). For the latter system, the two non-equivalent phase halves may be labelled the Al-terminated and Al-Zr-terminated half, respectively, depending on the identity of the last layer type before the defect plane, which now resides between two atomic planes. For the USF simulations with isolated Cu, the γ-surface calculations were modified to allow for full relaxation of the Cu NN atom positions. This procedure (see Supplementary Materials for a full discussion) preserved the extended defect while acknowledging that Cu triggers structural modulations along directions other than the APB plane normal, and was found to lower the single Cu partitioning energy by a non-negligible 0.11 eV. For the case of Cu pairing at the USF, implementation was prevented by simulation cell size constraints.

The calculated Cu mean partitioning energies at Al-Zr layers adjacent to a USF and an APB in $L1_2$-Al_3Zr are shown in Fig. 14(b) (for the sake of simplicity, the

presence of any Cu atoms away from these layers was ignored in the simulations). The process involving Cu replacement of Zr at the Al-Zr-terminated half next to the USF (purple diamonds in the figure) is found to represent the only seemingly realistic example of early Cu decoration (single Cu atoms and Cu pairs), with all alternative Cu placements at this stage producing mean partitioning energies close to 0.2 eV/Cu atom or higher. The partitioning energies for this preferred path remain slightly positive for the case of Cu pairing, but the sign here would almost certainly change if a model system with a larger defect plane area could be probed. There are no indications from the present calculations that the early stages of Cu agglomeration involve Al replacement. However, as the USF itself is a highly unfavorable defect (see Fig. 13(c)), a transition to the APB will ultimately occur. In this process, the configuration with Cu replacing Zr atoms only is strongly destabilized, and the full

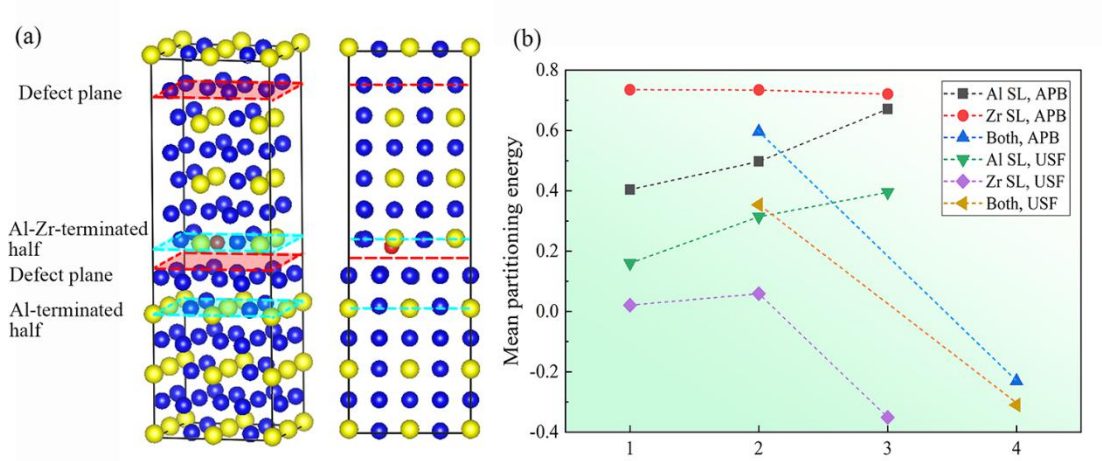

Cu decoration of one plane adjacent to the APB emerges as the most favorable configuration. Hence, theory and experiment appear to be in essential agreement. The results of Fig. 14(b) suggest that Cu can be attracted to the APB, provided that it manages to redistribute during the APB creation. In other words, a fundamental difference between the observations in Fig. 3, 4 is that the latter APB must have been created considerably more slowly.

Fig. 14 (a) Schematic illustration of a simulation cell used for modeling the interaction of Cu with a USF in $L1_2$-Al_3Zr. Compared to the APB in Fig. 13(a), the

defect plane is differently located, between two atomic layers, emphasizing symmetry breakage. The two Al-Zr planes closest to this defect plane have been highlighted in light blue. (b) Selected calculated Cu mean partitioning energies at Al-Zr layers adjacent to a USF and an APB in $L1_2$-Al_3Zr. The symbols highlight the identity of the extended defect and the decorated sublattice(s) within the proposed Cu layer. Four stages of Cu introduction are distinguished along the x-axis. 1: Single Cu atom; 2: Cu pair; 3, 4: Full Cu replacement for the specified set of sites.

4.4 $D0_{23}$ and Al_4CuZr phase stability

According to the experimental studies of this work, a transformation of $L1_2$-$Al_{3-x}Cu_xZr$ to either of the $D0_{23}$ and Al_4CuZr phases can occur upon prolonged heating at 500 °C, but ultimately (see Sec. 3.6), only the Al_4CuZr phase is observed. Theoretically, this transformation path has been probed in two steps: initially, it is asked whether a complete transformation of $L1_2$-$Al_{3-x}Cu_xZr$ to the $D0_{23}$-Al_3Zr phase is predicted, and subsequently, this question is repeated, with Al_4CuZr substituted for $D0_{23}$-Al_3Zr. $D0_{23}$-Al_3Zr is a stable phase in the Al-Cu-Zr equilibrium phase diagram, as ensured from Al-Zr phase diagram considerations. In order to see whether the introduction of $D0_{23}$-Al_3Zr implies the disappearance of $L1_2$-$Al_{3-x}Cu_xZr$, the formation energies of the latter phase are compared with the ($D0_{23}$-Al_3Zr)-Al_2Zr-Cu tie-plane energies (Fig. 15(a)). As shown in Fig. 15(c), $L1_2$ destabilization is predicted only for $C_{Cu,\ Al3Zr} < 5\%$. However, $L1_2$-$Al_{3-x}Cu_xZr$ particles with higher Cu content may still vanish from the alloy system under consideration upon the emergence of $D0_{23}$-Al_3Zr, as emphasized by the proposed ($D0_{23}$-Al_3Zr)-Cu tie-line in Fig. 15(a) crossing the ($L1_2$-$Al_{3-x}Cu_xZr$)-Al tie line favorably (and thus eliminating it) up to $C_{Cu,\ Al3Zr} \approx 11\%$ (see Fig. 15(d)). Incorporation of a configurational entropy term for the $Al_{3-x}Cu_xZr$ formation energies will reduce these $C_{Cu,\ Al3Zr}$ estimates non-negligibly, the latter possibly by even 5%. It therefore seems clear that the experimentally reported $L1_2$-$Al_{3-x}Cu_xZr$ dispersoids with $C_{Cu,\ Al3Zr} \approx 13\%$ should not vanish once $D0_{23}$-Al_3Zr forms. Rather, $D0_{23}$ is predicted to be a transient phase only. Experiment has reported the

incorporation of weak amounts of Cu in the $D0_{23}$ phase (see Sec. 3.2). As discussed in Supplementary Materials, theory suggests that $D0_{23}$-$Al_{3-x}Cu_xZr$ may appear in the Al-Cu-Zr phase diagram, but such configurations should not be stable in the alloy system under consideration, where Cu expulsion from $D0_{23}$ is always preferred. Hence, in connection with Fig. 15(a, c), $D0_{23}$-$Al_{3-x}Cu_xZr$ should always be a transient phase, with no influence on stability considerations.

To carry out corresponding theoretical investigations for the $L1_2 \rightarrow Al_4CuZr$ transition, the proposed Al_4CuZr structure of Sec. 3.4 was fully relaxed initially, with the result shown in Fig. 15(b). All structural parameters of Table 1 are found to be well reproduced by theory, with the computed cell dimensions being a = 11.85 Å, c = 4.036 Å. The composition Al_4CuZr is found to be located on the ($L1_2$-$Al_{3-x}Cu_xZr$)-Al-Cu tie-plane (see Fig. 15(e)). The Al_4CuZr phase formation energy of Table 2 falls well below this plane, suggesting that this phase is residing on the convex hull. Since the Al_4CuZr-Al tie-line will definitely exist, as it is not crossed by any existing tie-lines, it follows that the Al_4CuZr phase is expected to grow at the expense of $L1_2$-$Al_{3-x}Cu_xZr$ in the experimental alloy system. Thus, theory predicts that long-term heating leads to a pure Al_4CuZr microstructure (Fig. 15(f)), as observed experimentally.

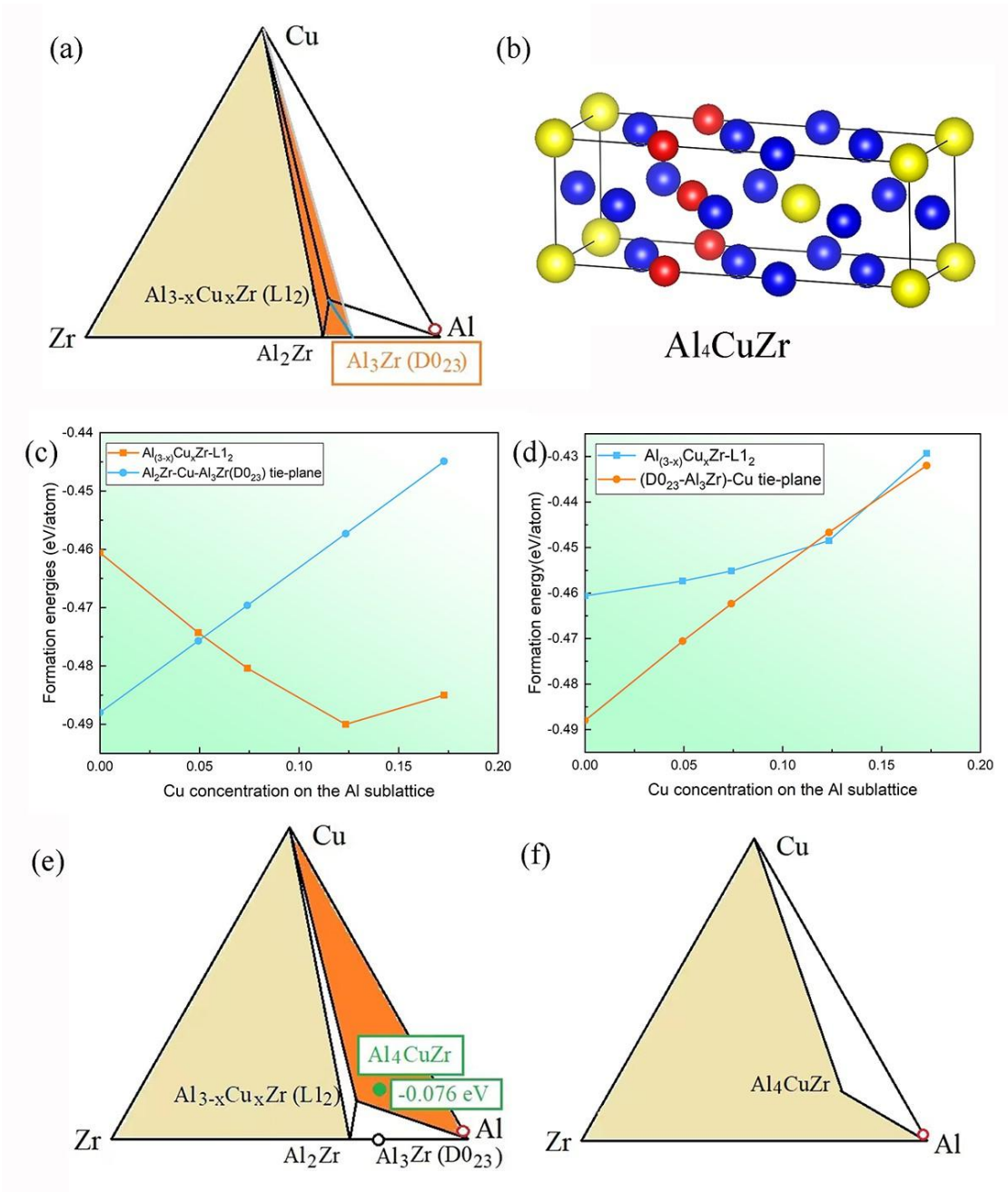

Fig. 15 (a) Hypothetical Al-Cu-Zr phase diagram describing the appearance of $D0_{23}$-Al_3Zr exclusively upon prolonged heating at 500 °C. Black lines are tie-lines linked to the $L1_2$-$Al_{3-x}Cu_xZr$ phase while the grey line describes a proposed ($D0_{23}$-Al_3Zr)-Cu tie-line. Additional nomenclature is explained in Fig. 12(b). (b) Schematic illustration of the fully relaxed Al_4CuZr structure. (c) Calculated $L1_2$-$Al_{3-x}Cu_xZr$ formation energies, compared to the ($D0_{23}$-Al_3Zr)-Al_2Zr-Cu tie-plane energies. (d) Calculated ($L1_2$-$Al_{3-x}Cu_xZr$)-Al tie-line energies, compared to the energies of the proposed ($D0_{23}$-Al_3Zr)-Cu tie-line at the (evolving) crossing point of these lines. (e) Comparison of

the Al_4CuZr formation energy with the ($L1_2$-$Al_{3-x}Cu_xZr$)-Al-Cu tie-plane. The green point indicates Al_4CuZr stability. (f) Al-Cu-Zr phase diagram showing the predicted phases upon long-term heating at 500 °C.

5. Discussion

5.1. Cu incorporation in $L1_2$-Al_3Zr

The present work has reported a Cu incorporation of ≈ 13% on the Al sublattice in $L1_2$-Al_3Zr. Despite some uncertainties in the calculated prediction of this value (see Sec. 4.1), theory is clearly in reasonable agreement. The Cu incorporation in $L1_2$-Al_3Zr observed in this work agrees with the findings of Hu et al. [30]. Since this value greatly exceeds other reports [28, 29], obtained for alloy systems with lower Cu content and subjected to different thermal treatment, a strong sensitivity for the Cu incorporation to one or both of these parameters is evident. Focusing on the observations of Schmid et al. [29], where the system under investigation did not contain alloying elements other than Cu and Zr, heating at 475 °C for 24h of a system containing 1.43 at.% Cu resulted in a hardly noticeable Cu presence in the dispersoids. In these experiments, large θ-Al_2Cu plates were still observed at the end of the heating process, whereas heating at 500 °C for the alloy system studied in the present work produced no Al-Cu phases. This difference means that the phase diagram of Fig. 12(b) should be altered when theoretically predicting the level of Cu incorporation in $L1_2$ for the alloy system in [29]. Following the line of strategy discussed in Sec. 4.1, $L1_2$-$Al_{3-x}Cu_xZr$ evidently will remain a phase on the convex hull: all Al-Cu phase formation energies lie above the $L1_2$-Al_3Zr energy, implying that the relevant tie-plane in the modified version of Fig. 12(c) will retain a positive slope. However, the modified tie-line consideration states (see Supplementary Materials) that at most 7% of Cu, and possibly notably less, will be introduced on the Al sublattice for the $L1_2$-$Al_{3-x}Cu_xZr$ particles that may be observed in the experimental alloy system. It follows that the presence of an Al_2Cu phase significantly reduces the Cu concentration in $L1_2$. The reason for the much higher Cu concentration in the dispersoids observed in the

present work and [30] may hence be proposed to be the choice of a heating temperature (500 °C) at which the Al_2Cu phase has been dissolved for the system under consideration.

5.2. Creation of an APB with no Cu decoration, and the $L1_2 \rightarrow D0_{23}$ transformation

The $L1_2 \rightarrow D0_{23}$ transformation is initiated by the formation of APBs without Cu decoration. These APBs are presumed to be created sufficiently fast for the Cu distribution on the Al sublattice to remain unchanged. As a result, the energy barrier to the APB creation is predicted to be raised notably with Cu content in $L1_2$ (see Fig. 13(c)), in agreement with experimental observations [26] that Cu incorporation increases the resistance of this phase to transformation, and thus stabilizes the $L1_2$ structure. The fully created APB will repel the Cu atoms as evidenced by the low Cu concentration in the $D0_{23}$ phase compared with $L1_2$, with the DFT calculations of Fig. 13(d) supporting this conclusion. As Cu is clearly mobile in $L1_2$ at 500 °C, even regions around isolated APBs turn Cu-poor, with a notably improved energy compared to the initial defect. Experimental studies suggest that such APB-hosting regions are favored relative to the defect-free Cu-hosting $L1_2$ phase, as evidenced by the APB area being increased as the particle starts changing shape from spherical to elongated (see Fig. 3(a)). Upon further particle evolution, the typical tendency for agglomerating APBs ($D0_{23}$ phase formation) may be explained, at least in part, by the fact that the Cu depletion around each APB creates a 'weak zone', particularly susceptible to transformation.

The theoretical studies of the APB creation do not probe the full interaction between the Al_3Zr particle and the Al matrix, but only the energy changes in the bulk precipitate. In these simulations, the "fast" creation of an isolated APB in an $L1_2$-$Al_{3-x}Cu_xZr$ dispersoid with $C_{Cu,\ Al3Zr}$ = 13% is predicted as unfavorable in Fig. 13(c), whereas the physical APB creation process is evidently associated with an energy gain. The likely reason for this discrepancy is an omitted interaction between dispersoid and matrix in the calculations, which in turn indicates that the APB

creation has an external origin. To the best of the author's knowledge, this topic is yet to be carefully addressed. Experimental observation has revealed the activation, at temperatures relevant to the Al_3Zr formation, of dislocations on {100} planes in pure Al and certain Al alloy systems [41, 42]. If such dislocations play a central role to the $L1_2 \rightarrow D0_{23}$ transformation, they would provide an additional stabilization (i.e., not taken into account in Sec. 4.2) of each created APB, linked to environmental stress field relief in the wake of the dislocation passage through the dispersoid. Such an energy contribution would also appear instrumental in explaining why $D0_{23}$ particles are observed in the present experiments, given that bulk phase theoretical studies (Sec. 4.4) predict this phase to be unstable relative to $L1_2$-$Al_{3-x}Cu_xZr$ at the observed values of $C_{Cu,\ Al3Zr}$. While a detailed study of this issue is outside the scope of this work, the key features observed in Fig. 3(a, c) for the $L1_2 \rightarrow D0_{23}$ transition arguably appear to require a full consideration of the particle-matrix interaction to be even qualitatively understood.

5.3. Creation of an APB with Cu decoration, and the $L1_2 \rightarrow Al_4CuZr$ transformation

As discussed in Sec. 3.3, Cu decoration of an APB in the $L1_2$ dispersoid may also occur. Such a scenario marks the onset of a transformation to the Al_4CuZr phase (by construction of a sheet of Al_4CuZr cells initially, see Fig. 5, 6). Upon heating for 300 h at 500 °C, a pure Al_4CuZr microstructure has emerged. This superior Al_4CuZr stability finds support in theory (see Sec. 4.4), with the DFT simulations further suggesting (Fig. 14(b)) that the Cu decoration is linked to the APB creation being sufficiently slow for Cu to redistribute during the process. Cu is found to be attracted to the USF (half completed APB), staying there as the extended defect fully transforms to the APB, with the predicted Cu decoration matching observation. When the APBs with Cu decoration are periodically activated within the dispersoid, the Al_4CuZr phase is formed. Frequently, $L1_2$, $D0_{23}$ and Al_4CuZr unit cells have been observed to coexist within one single particle, suggesting that a structural transformation from $L1_2$ to both $D0_{23}$ and Al_4CuZr occurs.

Altogether, the present work proposes the presence of a “branching” for the structural transformation of the $L1_2$-Al_3Zr phase in the presence of Cu. An illustration of the transformation rule is shown in Fig. 16. (i) When the APB creation is “fast”, the APB can repel the Cu atoms, resulting in a Cu-poor region being created around the APBs, and the creation of additional APBs will be increasingly likely in every other {100} plane next to the initial APB. In this way, the $D0_{23}$ phase is formed. (ii) Conversely, when the APB activation is “slowed down”, the Cu atoms are attracted to one plane adjacent to the APBs during the extended defect creation, replacing an array of Al and Zr columns and forming a Cu decorated layer. After the periodic arrangement of the Cu decorated layers is activated, the Al_4CuZr phase is formed, but this process is in natural competition with $D0_{23}$ creation, because the decorating atoms leave behind a comparatively Cu-poor vicinity promoting easier and faster APB creation (see Sec. 5.2). In other words, the two transformation paths can easily be simultaneously activated within one single particle. Only after heating for a long time do all the particles transform to the Al_4CuZr phase, either via internal transformation or dissolution. It is noted that the above discussion is not taking into consideration all details of the Al_4CuZr unit cell creation (Fig. 5). Those details are the planned study of future work.

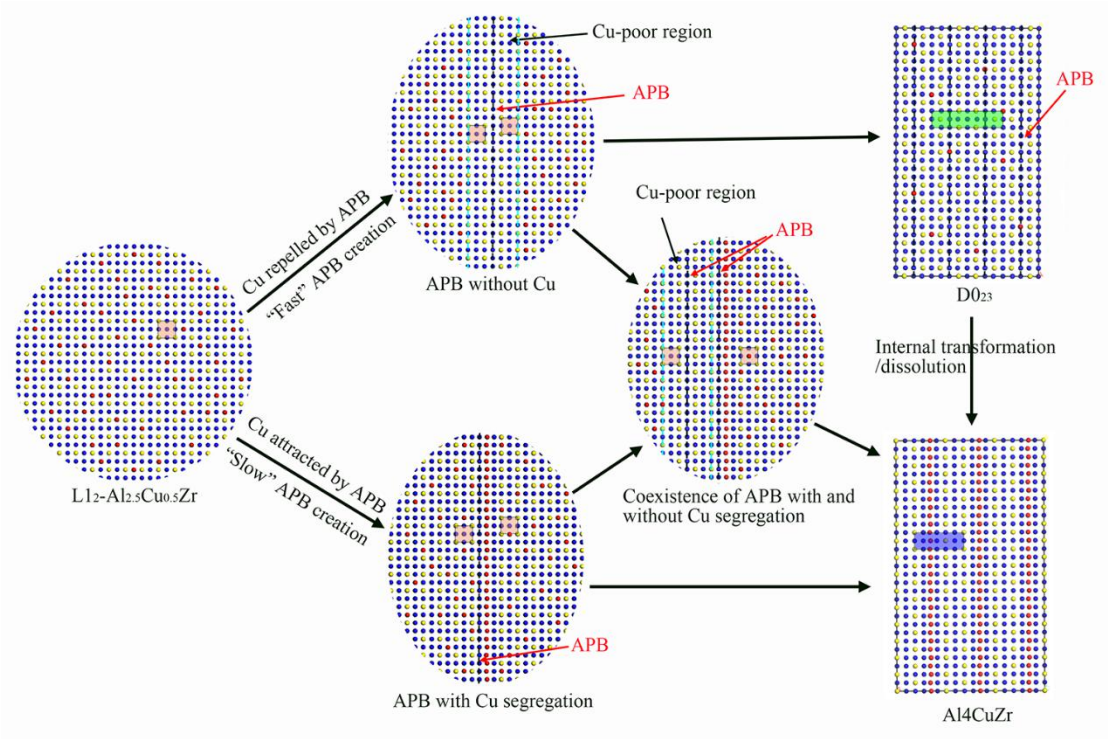

Fig. 16 Illustration of the transformation rule of the $L1_2$ phase to $D0_{23}$ or Al_4CuZr phase.

The appearance of the Al_4CuZr phase has not been reported in previous work. In the studies by Hu et al. [30], the duration of the heating process (26h) was almost certainly too short to trigger any Al_4CuZr formation (see Sec. 3.1). There are however indications from other experiments that this phase, while thermodynamically favored (see Fig. 15(e)), is comparatively challenging to nucleate. In the studies by Schmid et al. [29], Al_4CuZr was not observed even upon aging at 550 °C (for 24h) – a condition at which the transformation of $L1_2$ should be notably promoted. Instead, a relatively complete $L1_2 \rightarrow D0_{23}$ transformation was reported. That conclusion indicates that creation of Cu decorated APBs at an early stage of transformation of $L1_2$ is fundamental to the emergence of Al_4CuZr: A temporary promotion of the transition to $D0_{23}$ in [29] is not in itself surprising, as it may be explained by the lower Cu concentration in $L1_2$-$Al_{3-x}Cu_xZr$ (see Fig. 15(b, c)). However, if the order of creation of Cu decorated and Cu-free APBs were irrelevant, $D0_{23}$ should subsequently transform into Al_4CuZr by way of Cu attraction to the APBs, which does not appear to be the case. While further investigations into this issue would seem required, it is

conceivable that the studies of the present work have revealed a 'growth window' at which Al_4CuZr formation is possible. Since an increased Cu content in $L1_2$-$Al_{3-x}Cu_xZr$ raises the barrier to APB creation and hence slows down this process, it seems clear from the discussion in Sec. 5.1 that the chosen heating temperature during dispersoid formation would play a central role to such a growth window. A further examination into this issue is strongly encouraged for the purpose of examining Al_4CuZr nucleation optimization. From a more general perspective, it would be of interest to see if a similar branching of the $L1_2$ transformation path can be observed for the case of other micro-alloying elements. The present work has emphasized the possibility of a significantly changed evolution in the microstructure, apparently triggered essentially by the micro-alloying element managing to alter an extended defect (normally appearing in the dispersoid) during the stage of formation. If this mechanism has some level of generality to it, other entirely new phases may be grown in the same manner.

It is currently unclear how "fast" versus "slow" APB creation is to be understood quantitatively. Analysis of the $L1_2$ particle diameters have revealed no correlation between a preferred transformation to either $D0_{23}$ or coexisting $Al_4CuZr/D0_{23}$, meaning that a suspicion of larger particle sizes promoting the latter transformation has not found support. For an improved understanding of the nucleation and growth of Al_4CuZr, it would seem fundamental to clarify the full set of key factors promoting Cu decoration of the APB. The chemical mechanism explaining the Cu decoration of the APB is presently also unclear. The observed buckling of the Cu plane in Fig. 4(f) only provides a minute reduction (a few tens of a meV) to the Cu partitioning energy, and only the replacement of Zr with Cu at the USF triggers a clear reduction in the distances between the Al-Zr layers adjacent to the Cu layer. Both of these points indicate that Cu is trying to establish short bonds to Al. While this situation appears to resemble Al-Cu phase formation at first sight, it must be kept in mind that the valence electrons of Al in bulk $L1_2$-Al_3Zr have undergone significant hybridization in the process of bond formation with Zr, and hence are not chemically typical fcc Al atoms. Detailed electronic structure studies

were outside the scope of this work.

6. Conclusion

The influence of Cu on the precipitation of Al_3Zr dispersoids during solution treatment has been thoroughly studied in the present work, employing both atomic resolution high-angle annular dark-field scanning transmission electron microscopy, energy-dispersive X-ray spectroscopy and DFT simulations. It is revealed that the Cu atoms can significantly affect the stability and structural evolution of the Al_3Zr dispersoid during solution treatment. The following conclusions can be derived.

1. The Cu atoms are incorporated homogeneously in the interior of the $L1_2$-Al_3Zr particle, partially substituting the Al sublattice. In the present alloy system, the dispersoids were formed during solution treatment at 500 °C. The absence of Al-Cu phases at this condition allows for maximum Cu incorporation in the dispersoids for an Al-based alloy system, ≈ 13% according to both theory and experiment. The Cu incorporation decreases the lattice parameter of the $L1_2$ phase, almost eliminating the lattice misfit between dispersoid and Al matrix. Further, the Cu addition increases the energy barrier for APB activation by ≈ 50%, thus increasing the thermal stability of the $L1_2$ phase.

2. Upon additional solution treatment at 500 °C, Cu induces a "branched" path for the structural transformation of the $L1_2$-Al_3Zr phase. Firstly, the 'standard' ($L1_2 \rightarrow D0_{23}$ related) process may occur at which Cu is repelled by the APB. Secondly, the Cu atoms may preferentially segregate at the Al-Zr layer adjacent to the APB, forming a full Cu layer. These two very different outcomes can be linked, via a Suzuki effect, to the speed at which the APB is created. For the second path, this process is sufficiently slow that Cu has time to redistribute during APB formation. Following the initial APB creation, the dispersoid in general will be weakened in a region around this extended defect as a result of the

Cu-APB interactions and Cu mobility. Consequently, once defected, the $L1_2$ particle will be more susceptible to additional APB creations, i.e., the transformation will be accelerated.

3. After the periodic arrangement of the Cu decorated layers is activated in the particle, a new phase, referred to as the Al_4CuZr phase, is formed. Upon prolonged solution treatment at 500 °C, all dispersoids will transform to this phase. The Al_4CuZr phase has a tetragonal structure with lattice parameters a = 11.8 Å, b = c=4.04 Å and space group P4/nmm. This phase, which was computed to reside on the convex hull in the Al-Cu-Zr system, is reported here for the first time. Contrasting the $D0_{23}$ phase, the Al_4CuZr phase is fully coherent with the Al matrix. From this perspective, generation of an improved post-$L1_2$ microstructure may be possible if the Al_4CuZr formation can be further optimized.

Acknowledgements

This work was supported by the National Natural Science Foundation of China (Grant No. 52001159), the Natural Science Foundation of Jiangsu Province (BK20202010). We are grateful to the High Performance Computing Center of Nanjing Tech University for supporting the computational resources. H. Idrissi is mandated by the Belgian National Fund for Scientific Research (FSR- FNRS).

Reference

[1] J.-Y. Zhang, Y.-H. Gao, C. Yang, P. Zhang, J. Kuang, G. Liu, J. Sun, Microalloying Al alloys with Sc: a review, Rare Metals 39 (2020) 636-650.

[2] K.E. Knipling, R.A. Karnesky, C.P. Lee, D.C. Dunand, D.N. Seidman, Precipitation evolution in Al–0.1Sc, Al–0.1Zr and Al–0.1Sc–0.1Zr (at.%) alloys during isochronal aging, Acta Mater. 58 (2010) 5184-5195.

[3] K.E. Knipling, D.C. Dunand, D.N. Seidman, Criteria for developing castable,

creep-resistant aluminum-based alloys – A review, München Z. Metallkd 97 (2006) 246-265.

[4] M.S. Zedalis, M.E. Fine, Precipitation and Ostwald Ripening in Dilute AI Base-Zr-V Alloys, Metall. Trans. A 17 (1986) 2187-2198.

[5] K. Knipling, D. Dunand, Creep resistance of cast and aged Al–0.1Zr and Al–0.1Zr–0.1Ti (at.%) alloys at 300–400°C, Scr. Mater. 59 (2008) 387-390.

[6] Y.C.Chen, M.E.Fine, W. J.R, Microstructural evolution and mechanical properties of rapidly solidied Al-Zr-V alloys at high temperatures, Acta Metall. Mater. 38 (1990) 771-780.

[7] D. SRINIVASAN, K. CHATTOPADHYAY, Non-equilibrium Transformations Involving L12-Al3Zr in Ternary Al-X-Zr Alloys, Metall. Mater. Trans. A 36 (2005) 311-320.

[8] H. Lee, S.Z. Han, H.M. Lee, Z.-H. Lee, Coarsening behavior of L 12 precipitates in melt-spun A1-Ti-V-Zr alloys, Mater. Sci. Eng. A. 163 (1993) 81-90.

[9] K.E. Knipling, D.C. Dunand, D.N. Seidman, Precipitation evolution in Al–Zr and Al–Zr–Ti alloys during aging at 450–600°C, Acta Mater. 56 (2008) 1182-1195.

[10] S. Iwamura, Y. Miura, Loss in coherency and coarsening behavior of Al3Sc precipitates, Acta Mater. 52 (2004) 591-600.

[11] L.Potez, High-resolution electron microscopy studies of antiphase boundarie in Cu3Au, Inter. Sci. 2 (1994) 91-103.

[12] S. Pan, C. Li, F. Qian, L. Hao, Y. Li, Diffusion controlled early-stage L12-D023 transitions within Al3Zr, Scr. Mater. 231 (2023) 115460.

[13] K.E. Knipling, D.C. Dunand, D.N. Seidman, Precipitation evolution in Al–Zr and Al–Zr–Ti alloys during isothermal aging at 375–425°C, Acta Mater. 56 (2008) 114-127.

[14] G. Bester, M. Fähnle, Interpretation of ab initio total energy results in a chemical language: II. Stability of TiAl3 and ScAl3, J Phys-Condens. Mat. 13 (2001) 11551.

[15] J.-h. Xu, A.J. Freeman, Band filling and structural stability of cubic trialuminides: YAl3, ZrAl3, and NbAl3, Phys. Rev. B 40 (1989) 11927-11930.

[16] S.P. Wen, K.Y. Gao, H. Huang, W. Wang, Z.R. Nie, Precipitation evolution in

Al–Er–Zr alloys during aging at elevated temperature, J Alloy Compd. 574 (2013) 92-97.

[17] A. De Luca, D.C. Dunand, D.N. Seidman, Mechanical properties and optimization of the aging of a dilute Al-Sc-Er-Zr-Si alloy with a high Zr/Sc ratio, Acta Mater. 119 (2016) 35-42.

[18] C. Booth-Morrison, D.C. Dunand, D.N. Seidman, Coarsening resistance at 400°C of precipitation-strengthened Al–Zr–Sc–Er alloys, Acta Mater. 59 (2011) 7029-7042.

[19] W. Lefebvre, F. Danoix, H. Hallem, B. Forbord, A. Bostel, K. Marthinsen, Precipitation kinetic of Al3(Sc,Zr) dispersoids in aluminium, J Alloy Compd. 470 (2009) 107-110.

[20] A. Deschamps, L. Lae, P. Guyot, In situ small-angle scattering study of the precipitation kinetics in an Al–Zr–Sc alloy, Acta Mater. 55 (2007) 2775-2783.

[21] E. Clouet, L. Lae, T. Epicier, W. Lefebvre, M. Nastar, A. Deschamps, Complex precipitation pathways in multicomponent alloys, Nat. Mater. 5 (2006) 482-8.

[22] Y. Zhang, W. Zhou, H. Gao, Y. Han, K. Wang, J. Wang, B. Sun, S. Gu, W. You, Precipitation evolution of Al–Zr–Yb alloys during isochronal aging, Scr. Mater. 69 (2013) 477-480.

[23] T. Dorin, S. Babaniaris, L. Jiang, A. Cassel, C.P. Race, A. Eggeman, D.J. Kelly, S.J. Haigh, J.D. Robson, Stability and stoichiometry of L12 Al3(Sc,Zr) dispersoids in Al-(Si)-Sc-Zr alloys, Acta Mater. 216 (2021) 117117.

[24] D. Srinivasan, K. Chattopadhyay, Hardness of high strength nanocomposite Al–X–Zr (X=Si,Cu,Ni) alloys, Mater. Sci. Eng. A. 375-377 (2004) 1228-1234.

[25] J.D. Robson, A new model for prediction of dispersoid precipitation in aluminium alloys containing zirconium and scandium, Acta Mater. 52 (2004) 1409-1421.

[26] P.B. Desch, R.B. Schwarz, Formation of metastable L12 phases in Al-Zr and Al-2.5X-25%Zr(X = Li, Cr, Fe, Ni, Cu), J Less-Comm. Metals 168 (1991) 69-80.

[27] Z.-h. Jia, J.-P. CouziniÉ, N. Cherdoudi, I. Guillot, L. Arnberg, P. ÅSholt, S. Brusethaug, B. Barlas, D. Massinon, Precipitation behaviour of Al3Zr precipitate in

Al–Cu–Zr and Al–Cu–Zr–Ti–V alloys, T Nonferr. Metal Soc. 22 (2012) 1860-1865.

[28] A.M. Cassell, J.D. Robson, C.P. Race, A. Eggeman, T. Hashimoto, M. Besel, Dispersoid composition in zirconium containing Al-Zn-Mg-Cu (AA7010) aluminium alloy, Acta Mater. 169 (2019) 135-146.

[29] F. Schmid, D. Gehringer, T. Kremmer, L. Cattini, P.J. Uggowitzer, D. Holec, S. Pogatscher, Stabilization of Al3Zr allotropes in dilute aluminum alloys via the addition of ternary elements, Materialia 21(2022) 101321.

[30] H. Hu, M. Zhao, X. Wu, Z. Jia, R. Wang, W. Li, Q. Liu, The structural stability, mechanical properties and stacking fault energy of Al3Zr precipitates in Al-Cu-Zr alloys: HRTEM observations and first-principles calculations, J Alloy Compd. 681 (2016) 96-108.

[31] M. Zhao, Y. Xing, Z. Jia, Q. Liu, X. Wu, Effects of heating rate on the hardness and microstructure of Al-Cu and Al-Cu-Zr-Ti-V alloys, J Alloy Compd. 686 (2016) 312-317.

[32] S. P, Java electron microscopy simulation (JEMS) software, E´ cole Polytechnique Fe´de´rale de Lausanne Switzerland (2006).

[33] P.E. Blöchl, Projector augmented-wave method, Phys. Rev. B 50 (1994) 17953-17979.

[34] G. Kresse, D. Joubert, From ultrasoft pseudopotentials to the projector augmented-wave method, Phys. Rev. B 59 (1999) 1758-1775.

[35] J.P. Perdew, K. Burke, M. Ernzerhof, Generalized Gradient Approximation Made Simple, Phys. Rev. Lett. 77 (1996) 3865-3868.

[36] M. Methfessel, A.T. Paxton, High-precision sampling for Brillouin-zone integration in metals, Phys. Rev. B 40 (1989) 3616-3621.

[37] S. Kirklin, J.E. Saal, B. Meredig, A. Thompson, J.W. Doak, M. Aykol, S. Rühl, C. Wolverton, The Open Quantum Materials Database (OQMD): assessing the accuracy of DFT formation energies, npj Comput. Mater. 1 (2015) 15010.

[38] J.E. Saal, S. Kirklin, M. Aykol, B. Meredig, C. Wolverton, Materials Design and Discovery with High-Throughput Density Functional Theory: The Open Quantum Materials Database (OQMD), Jom 65 (2013) 1501-1509.

[39] W. Lefebvre, N. Masquelier, J. Houard, R. Patte, H. Zapolsky, Tracking the path of dislocations across ordered Al3Zr nano-precipitates in three dimensions, Scr. Mater. 70 (2014) 43-46.

[40] D.A. Porter, K.E. Easterling, M. Sherif, Phase Transformations in Metals and Alloys, CRC Press 2022.

[41] D. Tsivoulas, J.D. Robson, Heterogeneous Zr solute segregation and Al3Zr dispersoid distributions in Al–Cu–Li alloys, Acta Mater. 93 (2015) 73-86.

[42] M. Carrard, J. L. Martina, A study of (001) glide in [112] aluminium single crystals I. Creep characteristics, Phil. Mag. A 56(3) (1987) 391-405.